Technical University of Denmark

DTU

Mesoscale modeling for the Wind Atlas of South Africa (WASA) project

Hahmann, Andrea N.; Lennard, Chris; Badger, Jake; Vincent, Claire Louise; Kelly, Mark C.; Volker, Patrick; Argent, Brendan ; Nielsen, Joakim Refslund

Publication date:
2015

Document Version
Publisher's PDF, also known as Version of record

Link back to DTU Orbit

DTU Library
Technical Information Center of Denmark

Mesoscale modeling for the Wind Atlas of South Africa (WASA) project

Andrea N. Hahmann, Chris Lennard, Jake Badger,
Claire L. Vincent, Mark C. Kelly, Patrick J. H. Volker,
Brendan Argent and Joakim Refslund

Department of
Wind Energy
E Report 2014

DTU Wind Energy
Department of Wind Energy

Authors: Andrea N. Hahmann, Chris Lennard, Jake Badger, Claire L. Vincent, Mark C. Kelly, Patrick J. H. Volker, Brendan Argent and Joakim Refslund
Title: Mesoscale modeling for the Wind Atlas of South Africa (WASA) project

Summary (max 2000 characters):
This document reports on the methods used to create and the results of the two numerical wind atlases developed for the Wind Atlas for South Africa (WASA) project. The wind atlases were created using the KAMM-WAsP method and from the output of climate-type simulations of the Weather, Research and Forecasting (WRF) model, respectively.

The report is divided into three main parts. In the first part, we document the method used to run the mesoscale simulations and to generalize the WRF model wind climatologies, which was used for the first time in a wind atlas project. The second part compares the results from the numerical wind atlases (NWA) produced by the KAMM-WAsP with that produced with the WRF method, and verifies the two wind atlases from the two methods against the observed wind atlas (OWA) generated from wind observations from the 10 WASA masts. The KAMM-WAsP method was found to underestimate the generalized mean wind speeds at the sites (mean bias of -8.2% and mean absolute bias of 9.3%). In the WRF-based method there is, on average, a difference of 4.7% (either positive or negative) between the WRF-based NWA results and the corresponding observed values. The combined average across all the sites is an over-estimate of 2.5%. The report also documents the variability of the 62 m AGL wind speed at the 10 sites in the seasonal and diurnal time scale and compares it with the WRF-simulated winds.

DTU Wind Energy
Department of Wind Energy

Wind Atlas for South Africa (WASA)

Western Cape and parts of Northern and Eastern Cape

Mesoscale Modeling for the Wind Atlas of South Africa (WASA) Project

Andrea N. Hahmann, Jake Badger, Claire L. Vincent, Mark C. Kelly,
Patrick J. H. Volker and Joakim Refslund
Technical University of Denmark (DTU)

Chris Lennard and Brendan Argent
Climate Systems Analysis Group, University of Cape Town (UCT)
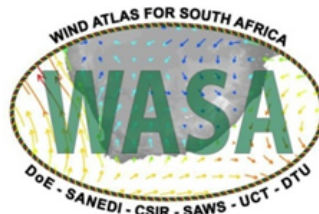
April 2014

Mesoscale Modeling for the Wind Atlas of South Africa (WASA) Project

Abstract

This document reports on the methods used to create and the results of the two numerical wind atlases developed for the Wind Atlas for South Africa (WASA) project. The wind atlases were created using the KAMM-WAsP method and from the output of climate-type simulations of the Weather, Research and Forecasting (WRF) model, respectively.

The report is divided into three main parts. In the first part, we document the method used to run the mesoscale simulations and to generalize the WRF model wind climatologies, which was used for the first time in a wind atlas project. The second part compares the results from the numerical wind atlases (NWA) produced by the KAMM-WAsP with that produced with the WRF method, and verifies the two wind atlases from the two methods against the observed wind atlas (OWA) generated from wind observations from the 10 WASA masts. The KAMM-WAsP method was found to underestimate the generalized mean wind speeds at the sites (mean bias of -8.2% and mean absolute bias of 9.3%). In the WRF-based method there is, on average, a difference of 4.7% (either positive or negative) between the WRF-based NWA results and the corresponding observed values. The combined average across all the sites is an over-estimate of 2.5%. The report also documents the variability of the 62 m AGL wind speed at the 10 sites in the seasonal and diurnal time scale and compares it with the WRF-simulated winds.

Contents

List of Figures

List of Tables

Chapter 1

Introduction

The conventional method used to produce estimates of wind resource over large areas or regions, such as on a national scale, is to analyze wind measurements made at a number of sites around the region, as in for example the European Wind Atlas (Troen and Petersen, 1989). In order for this method to work well there needs to be a sufficient quantity of high quality data, covering the country. This criterion is sometimes difficult to satisfy and therefore other methods are required that typically give good indications of the geographical distribution of the wind resource, and as such will be very useful for decision making and planning of feasibility studies.

Numerical wind atlas methodologies have been devised to solve the issue of insufficient wind measurements. Two methods are currently in use at DTU Wind Energy. One such methodology is the KAMM/WAsP method developed at Risø National Laboratory (Frank and Landberg, 1997). The other uses the Weather Research and Forecasting (WRF) model in a dynamical downscaling mode to produce mesoscale analysis. The two methods are described in the next chapter.

This report is structured as follows. Chapter 2 describes the method used for generating a wind atlas, both with the KAMM-WAsP and WRF mesoscale reanalysis methods. Chapter 3 describes the specific modeling setup for the KAMM-WAsP (Section 3.1) and WRF (Section 3.2) modeling systems used in the generation of the WASA numerical wind atlases (NWA). Chapter 4 presents the sensitivity experiments performed to find the best model configuration in the WRF mesoscale simulations. In Chapter 5 the validation of the KAMM and WRF-based numerical wind atlases against observations is presented. The results from the KAMM- and WRF-based numerical wind atlases are presented in Chapter 6. Finally, Chapter 7 presents a summary of the results and provides some conclusions.

Chapter 2

Methods

Numerical wind atlas methodologies have been devised to solve the issue of insufficient wind measurements. Two methods are currently in use at DTU Wind Energy. One such methodology is the KAMM/WAsP method developed at Risø National Laboratory (Frank and Landberg, 1997). The other uses the Weather Research and Forecasting (WRF) model in a dynamical downscaling mode to produce mesoscale analysis. The two methods are described in the next two sections.

2.1 The KAMM/WAsP method

In this methodology an approach called statistical-dynamical downscaling is used (Frey-Buness et al., 1995). The basis for the method is that there is a robust relationship between meteorological situations at the large-scale and meteorological situations at the small-scale. Information about the large-scale meteorological situation is freely available from the NCEP DOE 2 reanalysis data set. This dataset has been created by assimilating measurement data from around the globe in a consistent fashion from 1979 to the present day. The primary purpose for the generation of this dataset is to provide a reference for the state of the atmosphere and to identify any features of climate change. Another application of the dataset is as a long-term record of large-scale wind conditions. The NCEP DOE 2 reanalysis data is used to create around 100 different large-scale wind situations, called wind classes that represent the large-scale wind climate.

In order to make these wind classes meaningful at a smaller scale a mesoscale model is used to find out how the large-scale wind forcing is modified by regional scale topography. Therefore for each wind class a mesoscale model simulation is performed using the Karlsruhe Atmospheric Mesoscale Model (KAMM; Adrian and Fiedler, 1991).

Post-processing of the results from all the simulations yields a wind resource map at the resolution of the model simulations. Further analysis of the results from the simulations with consideration to the topography as described in the mesoscale model, yields wind atlas maps for generalized surface conditions. Files containing detailed information about the wind speed and direction distributions that are directly compatible with the WAsP software (Mortensen et al., 1999), the wind industry standard for site resource assessment.

2.2 The WRF Wind Atlas Method

The wind atlas method is based on the generalization of the wind climatologies derived from the mesoscale modeling. This generalization post-processing method has been used extensively in a number of wind resource assessment studies, particularly within the KAMM-WAsP method. This is the first wind atlas study were the generalization has been carried out on the WRF-model output.

    The post-processing allows a proper verification to be carried out, in which wind climate estimates derived from mesoscale modeling and measurements can be compared. Without the post-processing step no verification is possible, because the surface description within the model does not agree with reality, and therefore model winds will not agree with measured winds, except perhaps in extremely simple terrain or over water far from coasts.

2.2.1 Generalization factors

Four main parameters can be derived from the WRF model grid as described in Badger et al. (2014): (1) a factor that accounts for how the mesoscale model description of topography impacts the local flow, (2) a parameter that takes into account how the topography alters the mesoscale wind direction, (3) a parameter that accounts for the local flow perturbation on wind speed due to roughness length variations, and finally a (4) grid point dependent upstream roughness length. These four parameters are computed from the WRF grid description, that includes the topographic height and an average surface roughness length. These parameters are stored in a NetCDF file and used in the generalization of the WRF time series (see equations 2.1, 2.2 and 2.3).

2.2.2 Sectorization

Table 2.1 – Stability ranges and typical values used in the generalization procedure.

Stability class	Obukhov length range (m)	Typical Obukhov value $\tilde{L}$ (m)
Very unstable	-50 < L < -100	-75
Unstable	-100 < L < -200	-150
Near unstable	-200 < L < -500	-350
Neutral	L < -500; L > 500	10000
Near stable	200 < L < 500	350
Stable	50 < L < 200	125
Very stable	10 < L < 50	30

    To apply the generalization procedure to the WRF-model output, winds from the mesoscale model simulations are binned according to wind speed (usually in 2.5 m s^{-1} bins), wind direction (usually 48 sectors of 7.5° width) and seven stability class based on the Obukhov length that is also an output from the WRF simulation. The ranges for the stability classes are listed in Table 2.1 together with the "typical" length used in the generalization.

The procedure is carried out for each model grid point independently. In practice, time series of wind speed and direction at the desired vertical levels and $1/L$ are extracted from the model output files. The generalization procedure is then carried out on each time series file.

2.2.3 Basic generalization equations

In the first step, the time series of wind speed and direction are corrected for orography and roughness change, which are a function of wind direction and height. Given a time series of wind speed, $u = u(z, t)$, and wind direction, $\phi = \phi(z, t)$, which are functions of height and time, intermediate values, $\hat{u}$ and $\hat{\phi}$, are given by

$$\hat{u} = \frac{u}{(1 + \delta A_o)(1 + \delta A_r)} \tag{2.1}$$

$$\hat{\phi} = \phi - \delta\phi_o, \tag{2.2}$$

where δA_o, $\delta\phi_o$ and δA_r and are generalization factors for orography in wind speed and direction and roughness change, respectively, described in section 2.2.1 above. From the time series of corrected wind speed and direction "wind classes" are determined. The binning is based on wind direction sectors, wind speed and surface stability according to the Obukhov length as described in section 2.2.2. From the binning, mean values of wind speed, $\overline{u}$, and wind direction, $\overline{\phi}$ and typical Obuhov length $\tilde{L}$, together with the frequency of occurrence, F, of each bin are determined. For simplicity, we will drop the over-bar from the equations that follow, but it is understood that they are applied to the mean values of each bin and not the individual time series values.

From the corrected wind speed value we obtain an intermediary friction velocity, $\hat{u}_*$

$$\hat{u}_* = \frac{\kappa\hat{u}}{\ln[(z/\hat{z}_0) + \psi(z/\tilde{L})]} \tag{2.3}$$

where $\hat{z}_0$ is the downstream surface roughness length and ψ is a stability correction function that adjust the logarithmic wind profile due to non-neutral stability conditions and κ is the von Kármán constant. The stability correction uses the relationship:

$$\psi(z/L) = \begin{cases} -31.58[1 - \exp(-0.19z/L)] & \text{if } x \geq 0 \\ 2\log[0.5(1 + x)] + \log[0.5(1 + x^2)] - 2\tan^{-1}(x) + 1.5746 & \text{if } x < 0 \end{cases} \tag{2.4}$$

where $x = (1 - 19z/L)$. We use this function with a typical value of the Obukhov length from each wind class bin (see table 2.1). This procedure avoids using the similarity theory on wind profiles that lie outside the bounds of validity of the theory and that sometimes occur in the WRF simulations.

In the next step, we use the geostrophic drag law, which is used for neutral conditions to determine nominal geostrophic wind speeds, $\hat{G}$, and wind directions, α_G, are calculated, using the intermediate friction velocity and wind direction:

$$\hat{G} = \frac{\hat{u}_*}{\kappa} \sqrt{\left(\ln \frac{\hat{u}_*}{f \, \hat{z}_0} - A \right)^2 + B^2}, \tag{2.5}$$

$$\sin \hat{\phi}_G = -sin^{-1} \left(\frac{B \, \hat{u}_*}{\kappa \hat{G}} \right), \tag{2.6}$$

where $A = 1.8$ and $B = 5.4$ are two empirical parameters and f is the Coriolis parameter, and $\hat{\phi}_G$ is the angle between the near-surface winds and the geostrophic wind.

To obtain a new generalized friction velocity, $\hat{u}_{*G}$, for a standard roughness length $z_{0,std}$, Equation 2.5 is reversed by an iterative method,

$$\hat{G} = \frac{\hat{u}_{*G}}{\kappa} \sqrt{\left(\ln \frac{\hat{u}_{*G}}{f \, z_{0,std}} - A \right)^2 + B^2}, \tag{2.7}$$

Finally, the generalized wind speed, u_G, is obtained by using the logarithmic wind profile law

$$u_G = \frac{\hat{u}_{*G}}{\kappa \, ln(z/z_{0,std})}. \tag{2.8}$$

2.2.4 Weibull distribution fit

The frequency distribution of the horizontal wind speed can often be reasonably well described by the Weibull distribution function (Tuller and Brett, 1984):

$$F(u) = \frac{k_w}{A_w} \left(\frac{u}{A_w} \right)^{k_w - 1} \exp \left[- \left(\frac{u}{A_w} \right)^k \right], \tag{2.9}$$

where $F(u)$ is the frequency of occurrence of the wind speed u. In the Weibull distribution the scale parameter A_w has wind speed units and is proportional to the average wind speed calculated from the entire distribution. The shape parameter $k(\geq 1)$ describes the skewness of the distribution function. For typical wind speed distributions, the k_w-parameter has values in the range of 2 to 3.

From the values of A_w and k_w, the mean wind speed $\overline{U}$ (m s^{-1}) and mean power density $\overline{E}$ (W m^{-2}) in the wind can be calculated from:

$$\overline{U} = A_w \Gamma \left(1 + \frac{1}{k_w} \right) \tag{2.10}$$

$$\overline{E} = \frac{1}{2} \rho A_w^3 \cdot \Gamma \left(1 + \frac{3}{k_w} \right) \tag{2.11}$$

where ρ is the mean density of the air and Γ is the gamma function. We use the moment fitting method as used in the Wind Atlas Analysis and Application Program (WAsP) for estimating the Weibull parameters. The method is described in detail in Troen and Petersen (1989). Basically this method estimates A_w and k_w to fit the power density in the time series instead of the mean wind speed.

```
                                    WASA_wrf_32.856S_18.111E.lib
WASA_wrf    42   124    61 0.1000 <coordinates>18.11099,-32.85556,0.0</coordinates>
   5  5 12
 0.000 0.030 0.100 0.400 1.500
 10.0  25.0  50.0 100.0 200.0
11.39  2.24  1.26  1.10  3.40  7.45 24.14 28.33  4.75  3.66  4.14  8.15
 7.13  5.31  1.55  0.91  1.73  5.42  7.00 10.09  5.94  6.06  6.09  6.87
2.150 2.432 0.947 0.732 0.885 1.432 1.572 3.400 1.908 1.967 1.416 1.670
 8.26  5.04  2.63  2.47  2.71  5.71  7.75 10.50  6.60  6.50  6.22  8.01
3.268 1.783 1.393 1.846 1.209 1.436 1.705 2.365 2.139 2.111 1.369 2.029
 8.79  5.32  2.44  2.42  3.82  5.16  9.53 11.35  6.63  6.27  6.66  8.46
3.490 1.748 1.178 1.518 1.736 1.217 2.154 2.752 1.939 1.709 1.404 2.111
 8.79  6.40  3.27  2.66  3.83  7.10 10.72 12.79  6.08  6.26  6.90  8.93
2.076 1.643 1.365 1.229 1.256 1.658 2.229 3.607 1.451 1.506 1.283 1.982
10.16  8.82  3.85  2.99  5.27  7.95 12.64 12.70  5.85  5.28  6.67  9.17
1.971 1.369 1.127 1.189 1.396 1.463 2.365 2.275 1.213 1.100 1.104 1.627
 9.30  1.52  1.12  1.40  4.28  9.59 31.39 18.43  4.84  3.98  3.83 10.31
 4.73  2.38  1.04  1.65  1.31  4.29  6.45  6.71  4.38  4.78  3.62  5.41
1.787 1.100 0.838 1.850 0.787 1.447 1.955 2.607 1.752 2.049 1.037 1.963
 6.07  2.64  1.63  2.07  2.64  4.79  7.76  8.27  4.96  4.93  4.19  6.55
2.670 1.080 1.084 1.752 1.209 1.443 2.479 2.576 1.674 1.588 1.068 2.326
 6.93  3.85  1.84  1.91  2.93  5.59  9.10  9.29  5.36  5.38  5.35  7.61
2.771 1.533 1.092 1.287 1.217 1.607 2.666 2.795 1.654 1.654 1.244 2.803
 8.66  5.18  3.05  3.10  4.54  7.13 11.20 10.64  6.22  6.35  6.23  8.81
3.049 1.611 1.541 1.518 1.459 1.814 3.139 2.627 1.725 1.748 1.299 2.537
11.54  9.40  3.57  3.66  6.35 10.32 13.81 12.94  7.20  6.75  8.55 10.73
2.205 1.674 1.143 1.338 1.506 1.912 2.838 2.561 1.549 1.346 1.420 2.002
 9.20  1.89  0.96  1.91  5.06 12.68 33.25 13.13  4.33  3.82  4.17  9.59
 4.14  1.95  1.16  1.03  1.91  4.11  5.84  5.50  3.71  4.18  3.31  4.75
1.803 1.057 1.100 0.979 0.904 1.787 2.162 2.213 1.670 2.029 1.072 2.029
 5.54  2.20  2.00  2.10  3.24  4.09  6.91  7.14  4.57  4.41  4.10  5.69
```

Figure 2.1 – Structure of a WAsP "lib" file.

The Weibull fit is done for the ensemble of wind speeds in each wind direction bin (usually 12 direction sectors) for each standard height (usually 5 heights: 10, 25, 50, 100 and 200 m) and standard roughness lengths (usually 5 roughness: 0.0002 (water), 0.03, 0.1, 0.4, 1.5 m). The 25 Weibull fits for each wind direction sector use the method described above.

This sector-wise transformation of Weibull wind statistics—i.e. transforming the Weibull A_w and k_w parameters to a number of reference heights over flat land having given reference roughnesses—uses not only the geostrophic drag law, but also a perturbation of the drag law, with the latter part including a climatological stability treatment. The transformation and stability calculation is consistent with that implemented in WAsP and outlined in Troen and Petersen (1989), with further details given in Kelly and Troen (2014). The transformation is accomplished via perturbation of both the mean wind and expected long-term variance of wind speed, such that both Weibull-A_w and k_w are affected. When purely neutral conditions (zero stability effects) are presumed for the wind statistics to be transformed, there is still a perturbation introduced, associated with the generalized (reference) conditions in the wind atlas. This perturbation uses the default stability parameter values found in WAsP; it is negated upon subsequent application of the generalized wind from a given reference height and roughness to a site with identical height and surface roughness, using WAsP with its default settings. The climatological stability treatment in the generalization depends on the unperturbed Weibull parameters and effective surface roughness (Troen and Petersen, 1989), as well as the mesoscale output heights and wind atlas reference heights (though the latter disappears upon application of wind atlas data via WAsP).

Figure 2.1 shows the structure of the resulting WAsP "lib" file. It is structured as Weibull A_w's and k_w's for each sector, height and standard roughness length. The first row contains information about the geographical location of the wind climate represented in the lib-file. The second row lists the number of roughness classes (5), heights (5), and sectors (12), respectively. In the third and fourth row, the actual roughness (m) and heights (m) are listed. Below these header lines, a succession of frequencies of wind direction (1 line), values of
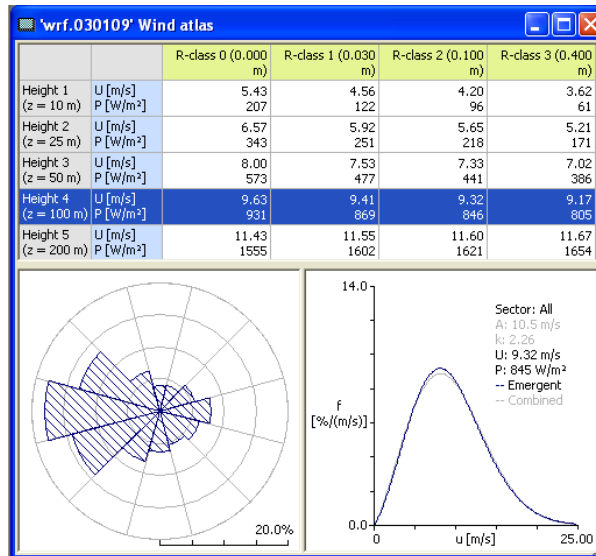
Figure 2.2 – Graphical view of a WAsP "lib" file.

Weibull-A_w (1 line) and Weibull-k_w (1 line) for each roughness class and height are printed for each sector (12 sectors per line). This type of file can be used and displayed (Figure 2.2) in WAsP.

2.3 Geostrophic drag law

The geostrophic drag law (GDL) relates the geostrophic wind, u_g, to the flow conditions at the surface, which are described by the friction velocity u_* and the surface roughness z_0. For homogeneous, neutral and barotropic conditions, the GDL is given by Eq. 2.5 (Gill, 1968). Usually, conditions are not homogeneous, neutral and barotropic, and the expressions for A and B in more complex conditions have been discussed by Floors (2013), Kristensen and Jensen (1999), Deacon (1973) and others.

Since the geostrophic drag law should relate the wind at the surface to that above the level at which the surface is 'felt', then it should be sensitive to the precise way in which energy is removed from the atmosphere by the drag forces at the surface. In the case of a mesoscale model, the way in which the surface interacts with the atmosphere is parametrized in the surface layer and boundary layer physics, and will not necessarily be the same as the relationships in the real atmosphere.

Several approaches could be taken to address this problem: A purely empirical, statistical relationship between the geostrophic wind, surface roughness and friction velocity could be developed. Or, the analytical form of the geostrophic drag law could be retained, but with new, model dependent values for A and B. We chose the second approach, since it retained the latitude dependence of relationship. Homogeneous, near-neutral, barotropic WRF simulations were used, where the geostrophic wind could be reliably calculated from the pressure gradient. Experiments were conducted for a range of surface roughness, geostrophic wind speeds and latitudes. Interestingly, it was found that fitting a single value of A and B for all latitudes gave inferior results, on average, than the standard values. On the other hand, fitting A and

B as linear functions of $\sin\phi$, where ϕ is the latitude, gave results with a similar overall error to using the standard values of A and B, but with somewhat different mean winds for the 10 verification sites.

2.4 Wind shear parameter

We use the power exponent parameter α defined from the power law:

$$u(z) = u_r \left(\frac{z}{z_r}\right)^{\alpha}, \tag{2.12}$$

where u_r and z_r are a reference wind speed and height. For a given set of heights, the value of α depends on atmospheric stability and roughness length. Alternatively, Eq. 2.12 can be rewritten as

$$\alpha = \frac{du}{dz}\frac{z}{u}. \tag{2.13}$$

We use the value of α as a diagnostic parameter for the wind shear in the surface layer.

Chapter 3

Mesoscale modeling

3.1 KAMM/WAsP

The KAMM/WAsP methodology used for the first verified wind atlas for WASA is called a statistical-dynamical downscaling. The basis for the method is that there is a robust relationship between meteorological situations at the large-scale and meteorological situations at the small-scale.

Information about the large-scale meteorological situation is freely available from the NCEP DOE II reanalysis data-set. Our application of this data-set is as a long term record of large-scale wind conditions. The NCEP DOE II data is used to create several different large-scale wind situations, called wind classes that represent the large-scale wind climate. Reanalysis data from 1980 to 2009 was used to calculate the 30-year large-scale climatological conditions.

In order to make the wind classes meaningful at a smaller scale the mesoscale model KAMM is used to find out how the large-scale wind forcing is modified by regional scale topography. An illustrative example of the KAMM domain is shown in Figure 3.1. For each wind class a KAMM mesoscale model simulation is performed. Post-processing of the results from all the simulations yields a wind resource map at the resolution of the model simulations at any chosen height above ground level. Further analysis of the results from the model simulations, with consideration to the topography, yields wind atlas maps for generalized surface conditions. Figure 3.2 offers a schematic flow diagram of the methodology. Files containing detailed information about the wind speed and direction distributions can be generated that are directly compatible with the WAsP software, the wind industry standard for site resource assessment calculations.

The WASA area of interest is larger than can be modelled with a single KAMM modelling domain. Therefore three KAMM modelling domains are defined to cover the area of interest. Figures 3.3 and 3.4 show the elevation and roughness length and coverage of the three calculation domains.

Three sets of wind classes are used to force the mesoscale model, for the SA2 (south-western), SA3 (south-eastern) and SA4 (north-western) domains respectively. These wind classes are shown in Figure 3.5, where each cross represents a forcing wind speed (distance from the centre of the diagram) and direction. The size of each cross represents the probability of the wind class. In fact the wind class probabilities vary slightly across the domain, as the atmospheric conditions vary across the domain, and the post-processing of the statistal-dynamical downscaling method accounts for this.
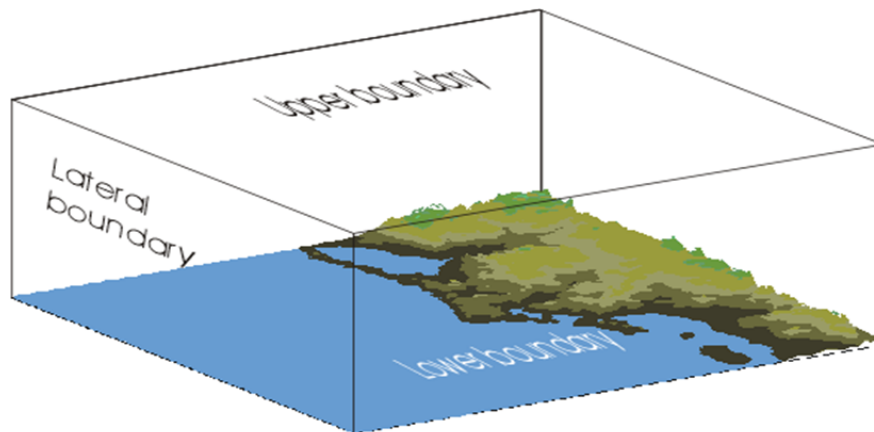
Figure 3.1 – Schematic diagram showing the KAMM modelling domain.
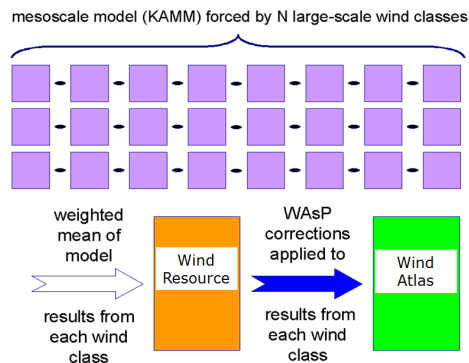
Figure 3.2 – Schematic diagram showing the KAMM/WAsP numerical wind atlas methodology. In this numerical wind atlas study, N, the number of wind classes is 84 for domain SA2 and SA3, and 137 for the domain SA4.

Each wind class set represents the distribution of domain characteristic wind speed, direction and temperature profiles, defined at 4 heights in the domain. For domains SA2 and SA3 the profiles are defined at heights 0, 1500, 3000, 5500 m above sea level. For the domain SA4 the profiles are defined at 0, 800, 1500, 5500 m above sea level. The difference in the way the profiles are defines for SA4 (north-western domain) was necessary in order to better capture an important shallow feature in the wind forcing at approximately 800 m, which would otherwise be missed.
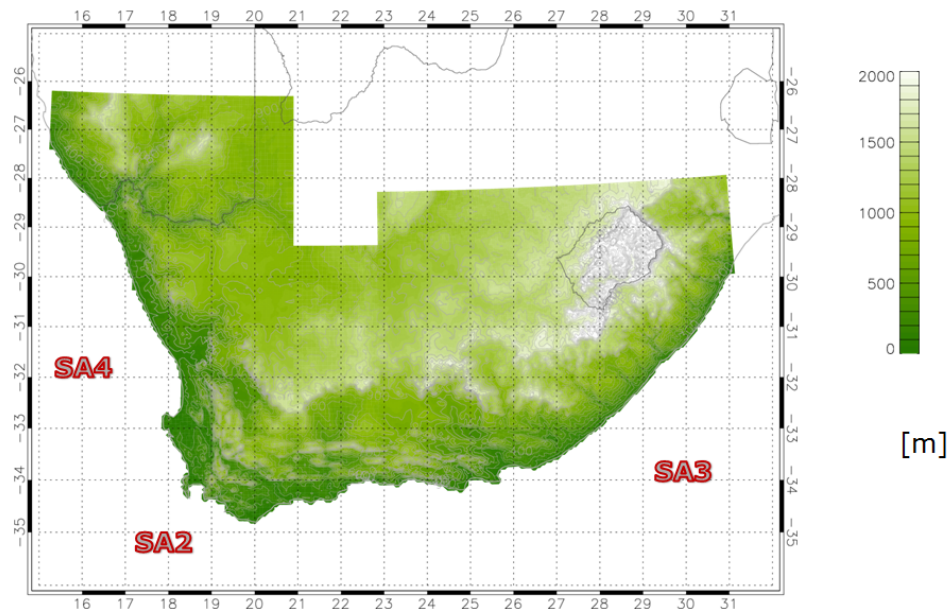
Figure 3.3 – The surface elevation over the three computational domains used for the KAMM mesoscale modelling at 5 km resolution for South Africa domains, labelled SA2, SA3 and SA4. The contour interval is 100 m. The x and y axis are degrees longitude and latitude. The data is derived from NASAâ Shuttle Radar Topography Mission (STRM) dataset version 2.
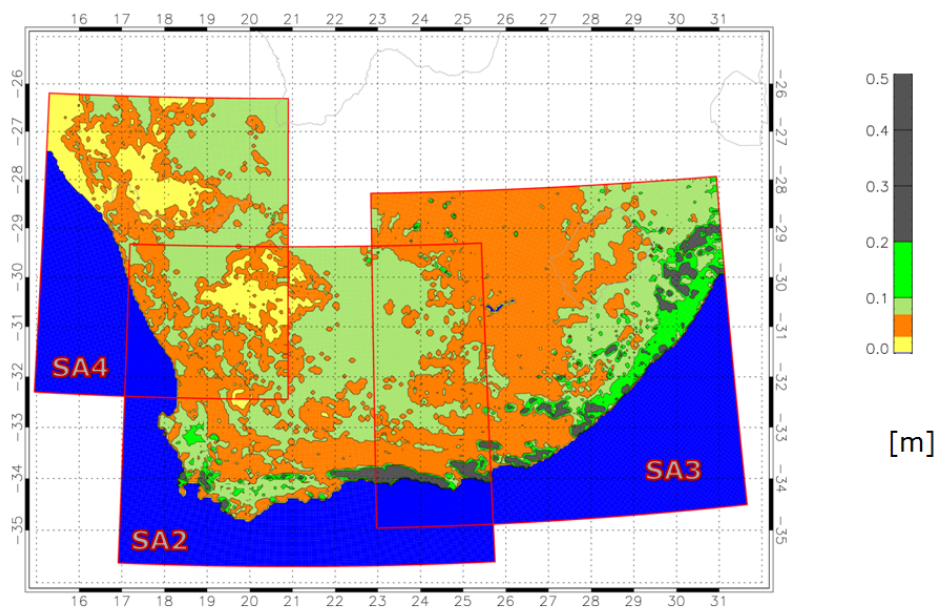
Figure 3.4 – The surface aerodynamic roughness length for the three modelling domains at a resolution of 5 km.The domains' boundaries are marked by the red lines, and labelled SA2, SA3, SA4. The x and y axes are degrees longitude and latitude . Colour key is given on the right hand side. The roughness data is derived from the United States Geological Survey (USGS) Global Land Cover Classification.
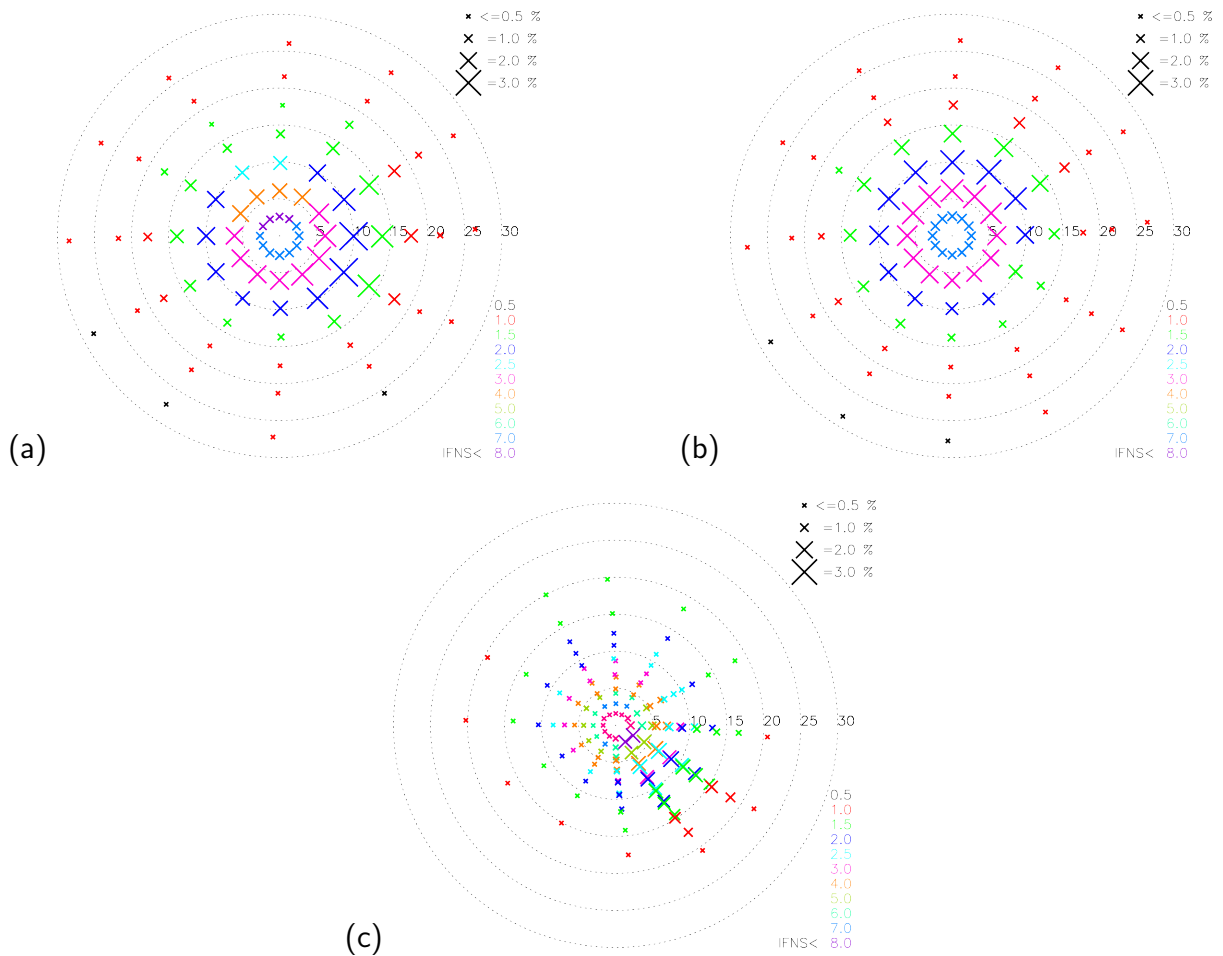
Figure 3.5 – The three sets of geostrophic wind classes for (a) SA2, (b) SA3, (c) SA4 based on NCEP DOE II reanalysis data for the period 1980–2009. Each cross represents a forcing wind speed (distance from the centre of the diagram) and direction. The speed scale is in m/s. The size of each cross represents the probability of the wind class. The frequency scale is given in the upper right hand corner. The color scale indicating the inverse Froude number squared (IFNS) is given in the lower right hand corner.

3.2 WRF Model description

The Weather, Research and Forecasting (WRF) Model (Skamarock et al., 2008) is a mesoscale numerical weather prediction system designed to serve both operational forecasting and atmospheric research needs. The simulations used to generate the WASA numerical wind atlas utilize the Advanced Research WRF (ARW-WRF) version 3.5.1 model released on 23 September 2013. The WRF modeling system is in the public domain and is freely available for community use. It is designed to be a flexible, state-of-the-art atmospheric simulation system that is portable and efficient on available parallel computing platforms. The WRF model is used worldwide for a variety of applications, from real-time weather forecasting, regional climate modeling, to simulating small-scale thunderstorms.

Although designed primarily for weather forecasting applications, ease of use and quality has brought the WRF model to be the model of choice for downscaling in wind energy applications. This model was used in wind-related studies concerning: wind shear in the North Sea (Peña and Hahmann, 2012) and over Denmark (Draxl et al., 2014), organized convection in the North Sea (Vincent et al., 2012), low-level jets in the central USA (Storm et al., 2009), wind climate over complex terrain (Horvath et al., 2012), gravity waves (Larsén et al., 2012), extreme winds (Larsén et al., 2013), among others.

3.2.1 Model setup

The final simulations for the WASA wind atlas were integrated on a grid with horizontal spacing of 21 km × 21 km (outer domain, D1, with 90 × 70 grid points), 9 km × 9 km (first nested domain, D2, with 184 × 133 grid points) and 3 km × 3 km (second nest, D3, with 426 × 310 grid points). A map of the model setup location, which was rotated to better cover the region of interest over southern Africa, is displayed in Fig. 3.6.

In the vertical the model was configured with 41 levels with model top at 50 hPa. The lowest 12 of these levels are within 1000 m of the surface and the first level is located at approximately 14 m AGL. Table 3.1 list the details of the model configuration, including the model parametrizations used in the simulations. The actual namelist used in the simulations is presented in Appendix A.
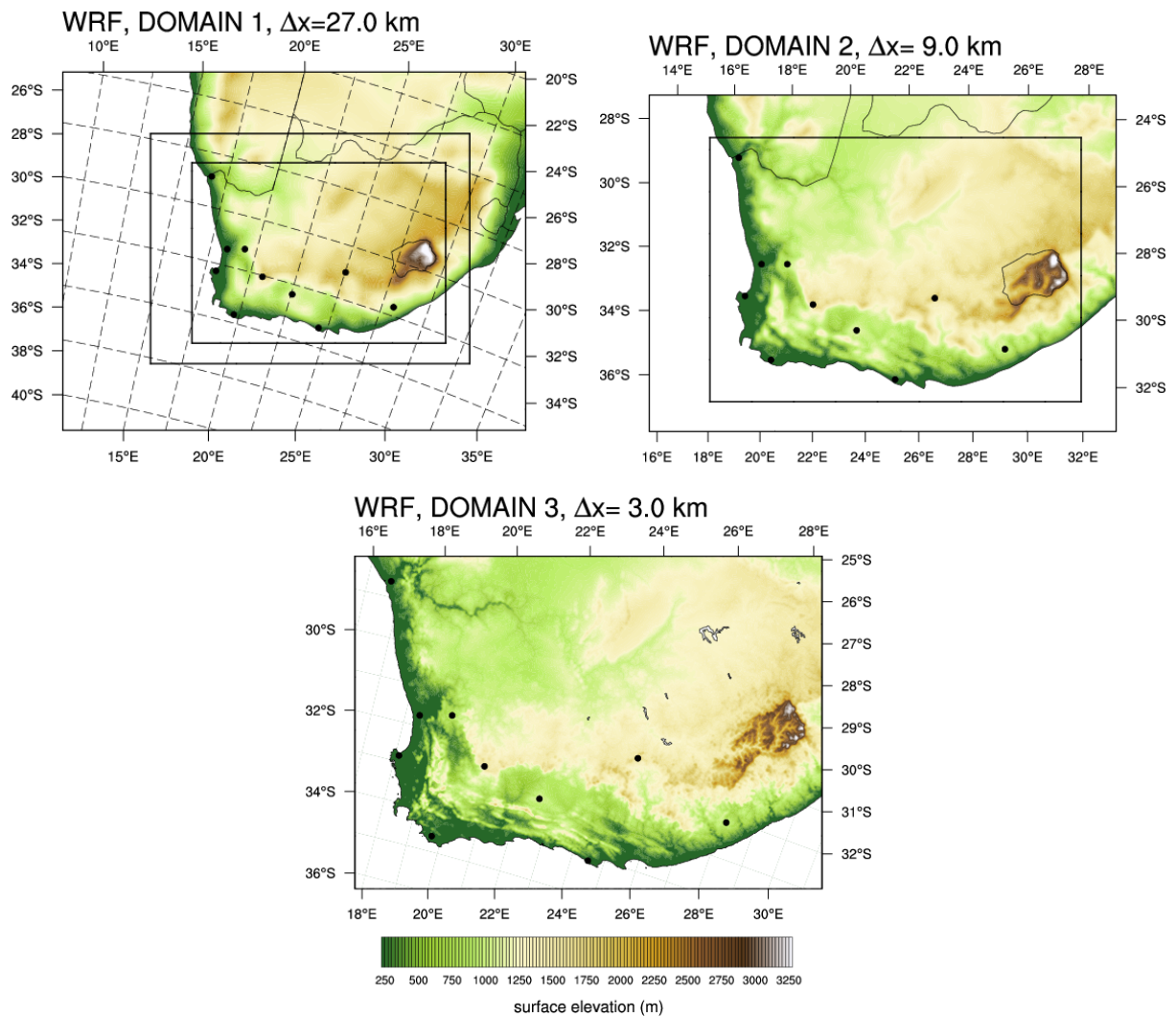
Figure 3.6 – WRF model domains configuration and terrain elevation (m). Top left: 27 km × 27 km domain (D1), Top right: 9 km x 9 km (D2) and Bottom: 3 km × 3 km (D3). The inner lines show the position of D2 and D3 in D1 and D2, respectively. The location of the WASA masts is shown by the dots.

Table 3.1 – Summary of model and system setup and physical parameterizations used in the control main WASA simulations.

Model setup:
WRF (ARW) Version 3.5.1.
Mother domain (D1; 90 × 70 grid points) with 27 km grid spacing; 2 nested domains: D2 (184 × 133 grid points) using 9 km and D3 (426 × 310 grid points) horizontal grid spacing on a Lambert conformal projection (see Fig. 3.6).
41 vertical levels with model top at 50 hPa; 9 of these levels are placed within 1000 m of the surface; The first 6 levels are located approximately at: 14, 43, 72, 100, 129 and 190 m.
MODIS (2001–2010) land-cover classification of the International Geosphere-Biosphere Programme.
Simulation setup:
Initial, boundary conditions, and fields for grid nudging come from the European Centre for Medium Range Forecast (ECMWF) ERA-Interim Reanalysis (Dee et al., 2011) at $0.7° \times 0.7°$ resolution.
Runs are started (cold start) at 00:00 UTC every 10 days and are integrated for 11 days, the first 24 hours of each simulation are disregarded.
Sea surface temperature (SST) and sea-ice fractions come from the dataset produced at USA NOAA/NCEP at $1/12° \times 1/12°$ resolution (Gemmill et al., 2007) and are updated daily.
Model output: hourly (lowest 11 vertical levels) for D3, 3-hourly for D1 and D2, wind speeds at 7 vertical levels every 10 minutes for D3 only. Time step in most simulations: approx. 160 seconds.
One-way nested domains; 5 grid point nudging zone.
Grid nudging on D1 only and above level 15; nudging coefficient 0.0003 s^{-1} for wind, temperature and specific humidity. No nudging in the PBL.
Physical parameterizations:
Precipitation: WRF Single-Moment 5-class scheme (option 4), Kain-Fritsch cumulus parameterization (option 1) turned off on D3.
Radiation: RRTM scheme for longwave (option 1); Dudhia scheme for shortwave (option 1)
PBL and land surface: Mellor-Yamada-Janjic scheme (Mellor and Yamada, 1982) (option 2), Eta similarity (option 2) surface-layer scheme, and Noah Land Surface Model (option 2).
Surface roughnesses are kept constant at their winter (lower) value.
Diffusion: Simple diffusion (option 1); 2D deformation (option 4); 6th order positive definite numerical diffusion (option 2); rates of 0.06, 0.08, and 0.1 for D1, D2, and D3, respectively; vertical damping.
Positive definite advection of moisture and scalars.

Most choices in the model setup are fairly standard and used by other modeling groups. The only special setting for wind energy applications is the use of a constant surface roughness length, thus disabling the annual cycle available in the WRF model. This choice is consistent with the generalization procedure discussed in section 2.2.

The final simulation covered the period October 2005 – September 2013, and were run in a series of 11-day long overlapping simulations, with the output from the first day being discarded. This method is based on the assumptions described in Hahmann et al. (2010). The simulation used grid nudging that continuously relaxes the model solution towards the gridded reanalysis but this was done only on the outer domain and above the boundary layer (level 15 from the surface) to allow for the mesoscale processes near the surface to develop freely. Because the simulations were re-initialized every 10 days, the runs are independent of each other and can be integrated in parallel reducing the total time needed to complete a multi-year climatology. The grid nudging and 10-days reinitialization keeps the model solution from drifting from the observed large-scale atmospheric patterns, while the relatively long simulations guarantee that the mesoscale flow is fully in equilibrium with the mesoscale characteristic of the terrain. One major change to the standard WRF modeling system was the change in landuse (and its associated surface roughness length) for the WASA simulations. Detailed inspection of the standard landuse maps in WRF showed serious problems.
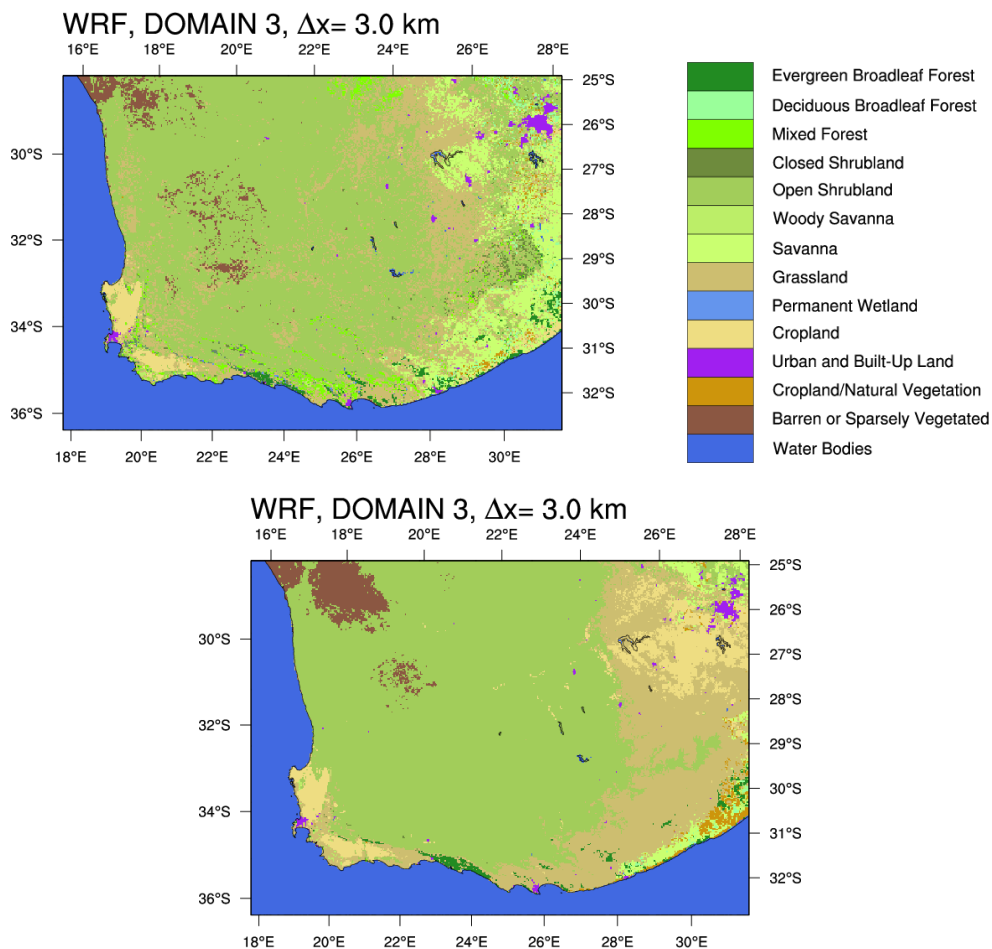
Figure 3.7 – Comparison of WRF landuse map in the standard WRF derived from MODIS Collection 4 (top) and the updated using updated MODIS Collection 5, 2001–2010 landuse (bottom).

3.2.2 Updated vegetation

From the MODIS product documentation[1] reports significant problems in the training data which may have serious consequences for the classified data. These regions include the savannas of South Africa misclassifying open shrubland as savanna. The same document reports that overall previous versions of the MODIS-based data still overestimated forest cover in most areas and under-classifying woody savanna due to deficiencies within the training data. Newer versions of the dataset, such as the one used to generate the lower map in Fig. 3.7, show improvements over previous versions.

For the WASA final simulation we used an "averaged" landuse map for the period 2001–2010 derived from MODIS Collection 5 (Friedl et al., 2010), as opposed to the MODIS C4-based data from a single year for 2001.

Surface roughness were modified from those used in the standard WRF V3.6.1 setup. The new values are presented in Table 3.2. In addition to the new values, the annual variation in surface roughness used in WRF was disabled by setting the minimum and maximum values to a single value. The resulting surface roughness map is presented in Fig. 3.8.

Table 3.2 – Surface roughness length as a function of landuse class for the standard WRF (minimum and maximum) and the modified for the WASA simulations.

MODIS Landuse class	Min/Max stand roughness (m)	New roughness (m)
Evergreen Broadleaf Forest	0.50/0.50	0.50
Deciduous Broadleaf Forest	0.50/0.50	0.50
Mixed Forests	0.20/0.50	0.35
Closed Shrublands	0.01/0.05	0.03
Open Shrublands	0.01/0.06	0.03
Woody Savannas	0.01/0.05	0.03
Savannas	0.15/0.15	0.15
Grasslands	0.10/0.12	0.10
Croplands	0.05/0.15	0.10
Urban and Built-Up	0.50/0.50	0.50
Cropland/natural vegetation mosaic	0.05/0.14	0.055
Barren or Sparsely Vegetated	0.01/0.01	0.01

3.2.3 Data processing

Wind speeds and directions are derived from the WRF model output, which represents 10-minutes or hourly instantaneous values. For evaluating the model wind speed climatology, the zonal and meridional wind components on their original staggered Arakawa-C grid were interpolated to the coordinates of the mass grid. The interpolated wind components were then used to compute the wind speed and rotated to the true north to derive the wind direction. For a given height, e.g., 100 m, wind speeds are interpolated between neighboring model

---

[1]http://daac.ornl.gov/MODIS/MODIS-menu/MCD12Q1_known_issues.html
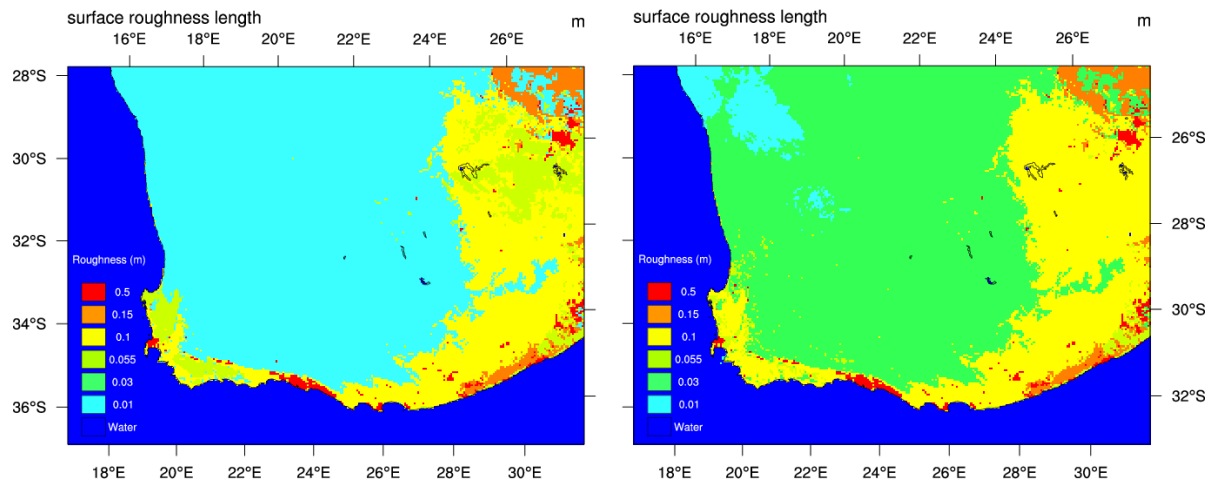
Figure 3.8 – Map of surface roughness length (m) for South Africa based on MODIS 2001 C4 in winter (left) and MODIS 2001–2010 C5 (right)

levels using logarithmic interpolation in height. It was found that this interpolation procedure preserves more of the original features in the model wind profile compared to other schemes (e.g., linear or polynomial interpolation of the wind components).

For the entire WASA domain, which contains 39,713 grid-points, time-series for the entire period (421,200 10-minute events) for the wind speed, wind direction at 5 heights, and $1/L$ were generated. The generation of the time-series was a very time consuming process because the WRF output files are stored for every three hours for the whole domain. The generation of time-series requires that for every grid-point in the considered region all files for the whole period have to be accessed. The problem is that the single point extraction from the large WRF output files is relatively time consuming and that this process has to be repeated in time for the whole region.
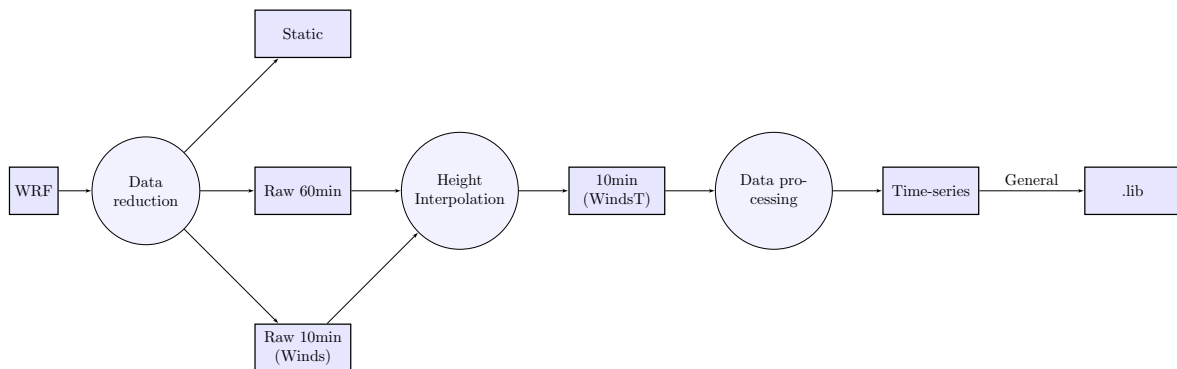
Figure 3.9 – Schematic representation of the data processing used to create the wind climate files that compose the WRF-based NWA.

Chapter 4

Sensitivity Experiments

An extensive series of sensitivity experiments were carried out to determine the best model configuration for the WASA experiments. The multi-physics experiments were carried out with a single domain configuration. The effect of model position and grid spacing was also investigated.

4.1 Multi-physics experiments

The multi-physics experiments were carried out with a 5 km $\times$ 5 km inner grid domain. The grid used was Lambert projection centered at 30°S, 22°E rotated to provide maximum coverage over South Africa. Domain 1: $\Delta x = \Delta y = 45$ km, 96 $\times$ 72 grid points; Domain 2: $\Delta x = \Delta y = 15$ km, 163 $\times$ 118 grid points; Domain 3: $\Delta x = \Delta y = 5$ km, 292 $\times$ 217 grid points. The grid location is shown in Fig. 4.1.

The description of the experiments is shown in Table 4.1. Most experiments were conducted for a period of 13 months (1 September 2010 – 30 September 2011). A few experiments exhibited very low sensitivity and thus were discontinued after 3 or 4 months.
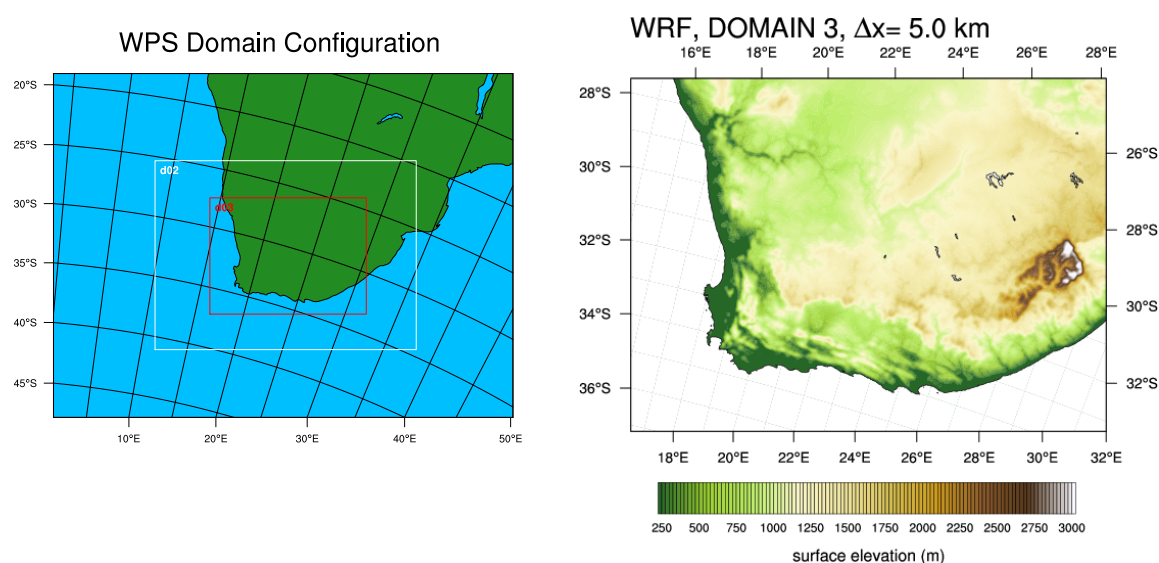
Figure 4.1 – Model configuration used in the multi-physics sensitivity experiments: Domain configuration (left) and D3 domain elevation (right).

Table 4.1 – Summary of the wind atlas simulations performed on the 5 km × 5 km grid.

Exp. Name	Microphysics	Longwave	Shortwave	Land Surface	Surface layer	PBL	Cum	Period	Notes
ERA	WSM 5-class	RTMG	RTMG	Noah	ETA sim	MYJ	K-F	1 year	
CFSR	WSM 5-class	RTMG	RTMG	Noah	ETA sim	MYJ	K-F	1 year	
ERA_YSU	WSM 5-class	RTMG	RTMG	Noah	MM5 sim	YSU	K-F	1 year	
ERA_RRTMG	WSM 5-class	RRTMG	RRTMG	Noah	ETA sim	MYJ	K-F	1 year	
ERA_THOM	Thompson	RTMG	RTMG	Noah	ETA sim	MYJ	K-F	4 months	low sens
ERA_KF	WSM 5-class	RTMG	RTMG	Noah	ETA sim	MYJ	K-F	4 months	K-F in D3 (low)
ERA_ULCC	WSM 5-class	RTMG	RTMG	Noah	MM5 sim	YSU	K-F	1 year	new land & ZNT
ERA_PLX	WSM 5-class	RTMG	RTMG	PLX	Pleim-Xiu	ACM2	K-F	1 year	diff land
ERA_PLX_YSU	WSM 5-class	RTMG	RTMG	PLX	MM5 sim	YSU	K-F	3 months	(low)
ERA_YSU_RRTMG	WSM 5-class	RRTMG	RRTMG	Noah	MM5 sim	YSU	K-F	1 year	

Table 4.2 – Summary of the Figure number where the difference between the two simulations in Table 4.1 is displayed.

Simulation name	ERA	ERA_YSU
CFSR	Fig. 4.2a	
ERA_YSU	Fig. 4.2b	
ERA_RRTMG	Fig. 4.2c	
ERA_YSU_RRTMG		Fig. 4.2d
ERA_THOM	Fig. 4.2e	
ERA_KF	Fig. 4.2f	
ERA_ULCC	Fig. 4.3a	
ERA_PLX	Fig. 4.3b	
ERA_PLX_YSU		Fig. 4.3c

Figure 4.2a shows the difference in annual mean wind speed between the simulation forced by the ERA Interim reanalysis and the CFSR reanalysis. The simulation using the CFSR reanalysis has slightly larger wind speeds (with a maximum difference of around 0.5 m s^{-1}) over the interior of South Africa. No significant differences are found at any of the verification sites. The differences when using the YSU PBL scheme compared to the MYJ PBL scheme (Fig. 4.2b) are also very small.

The next set of experiments explores the role of the radiation parameterization. Two experiments were conducted: one with the RRTMG scheme and the MYJ parameterization (Fig. 4.2c another with the same radiation scheme but using the YSU parameterization (Fig. 4.2d). Neither experiments shows absolute differences larger than about 0.5 m s^{-1}, but interestingly the differences are negative when using the MYJ scheme and positive when using the YSU scheme.

The next two experiments tested the effect of the explicit moisture scheme (Fig. 4.2e) and convective scheme in D3 (Fig. 4.2f). These two sets are virtually insensitive with regards to the annual mean averaged wind speed.

The experiments explore the role of changes in land use and surface roughness length, and the land surface model. The difference between the ERA simulation and the ERA_ULCC is shown in Fig. 4.3a. Due to the reduced roughness in the ERA_ULCC simulation, wind speeds are generally larger (0.25–0.8 m s^{-1}) over most western land areas.

The largest impact of any of the sensitivity experiments is due to the use of a different land surface model (Figs. 4.3b and 4.3c). Differences in annually averaged wind speed are as large as 2 m s^{-1} in some areas, especially over the northwest coast. Part of these differences are attributable to changes in surface roughness (not shown), but also probably to the treatment of the surface fluxes and the resulting wind shear. The standard PLX land surface model is ran with a different PBL scheme, the ACM2 PBL scheme. To explore how much of the seen differences are related to the PBL parameterization, a new experiment was carried out using the PLX land surface model, but the YSU PBL scheme. The differences in annual mean wind speed between these two experiments in Fig. 4.3c are small. This leads us to conclude that it is the land surface model, and not the PBL scheme, that is responsible for the large wind speed differences in Fig. 4.3b.

(a) ERA - CFSR

(b) ERA (MYJ) - ERA_YSU

(c) ERA - ERA_RRTMG

(d) ERA_YSU - ERA_YSU_RRTMG

(e) ERA - ERA_THOM (4 months)

(f) ERA - ERA_KF (4 months)
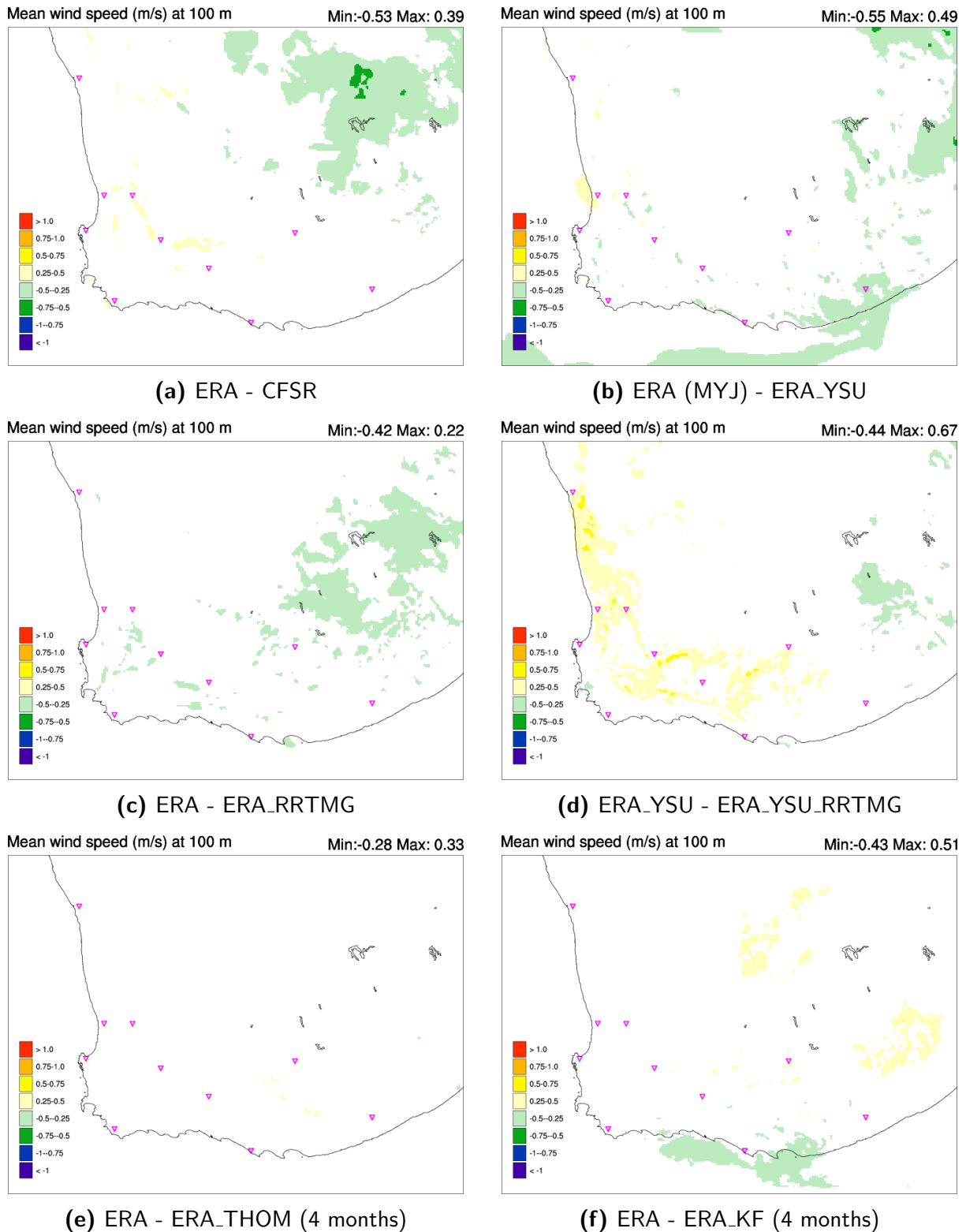
Figure 4.2 – Difference in annually averaged wind speed $(\mathrm{m\,s^{-1}})$ at 100 m AGL between two simulations for the period 1 October 2010 – 30 September 2011, except for (e) and (f) for 1 October 2010 – 31 January 2011. The pink triangles show the locations of the WASA masts.

(a) ERA - ERA_ULCC

(b) ERA - ERA_PLX

(c) ERA_PLX - ERA_PLX_YSU (3 months)
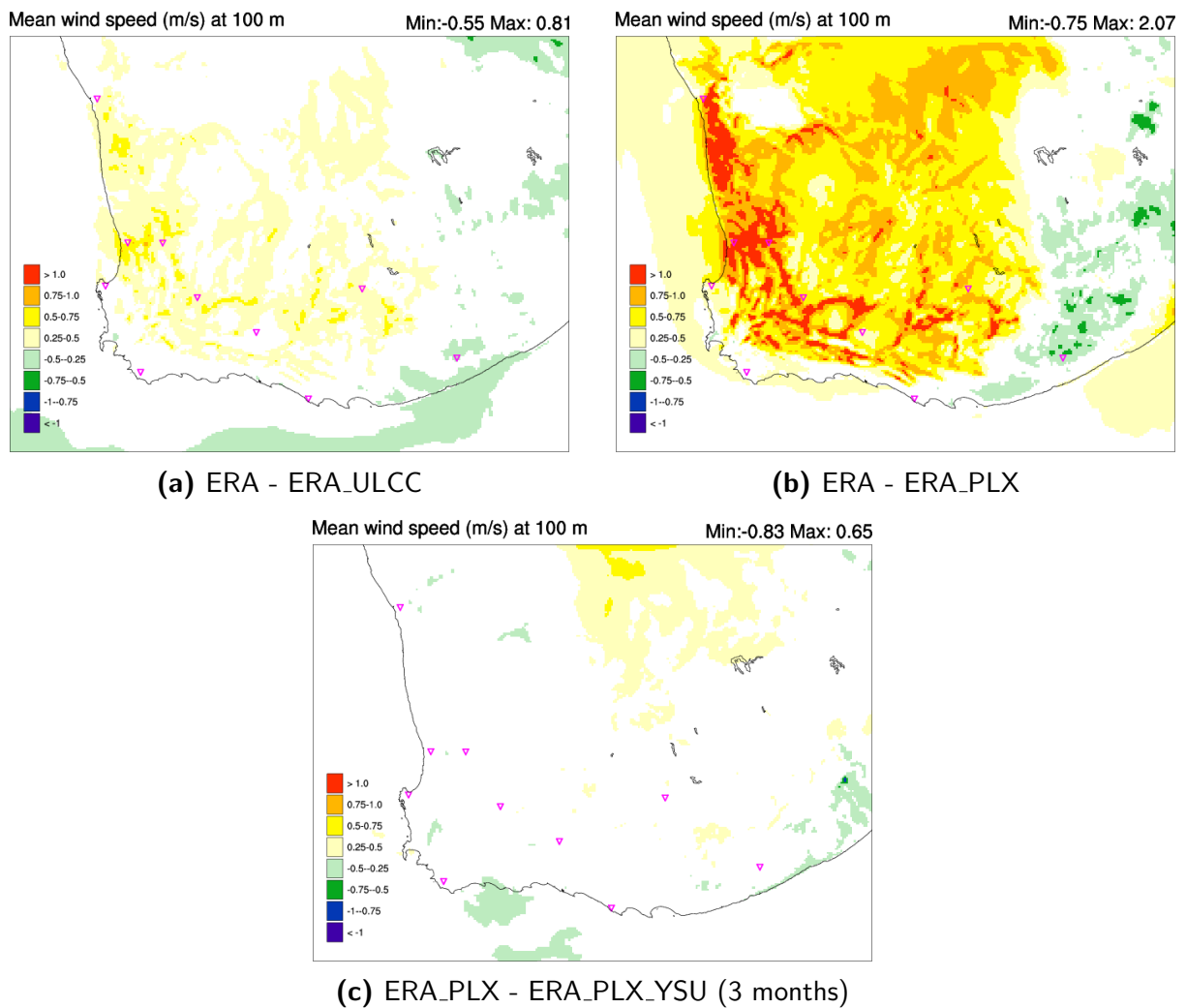
Figure 4.3 – Difference in annually averaged wind speed $(\mathrm{m\,s^{-1}})$ at 100 m AGL between two simulations for the period 1 October 2010 – 30 September 2011, except for (c) for 1 October – 31 December 2011. The pink triangles show the locations of the WASA masts.
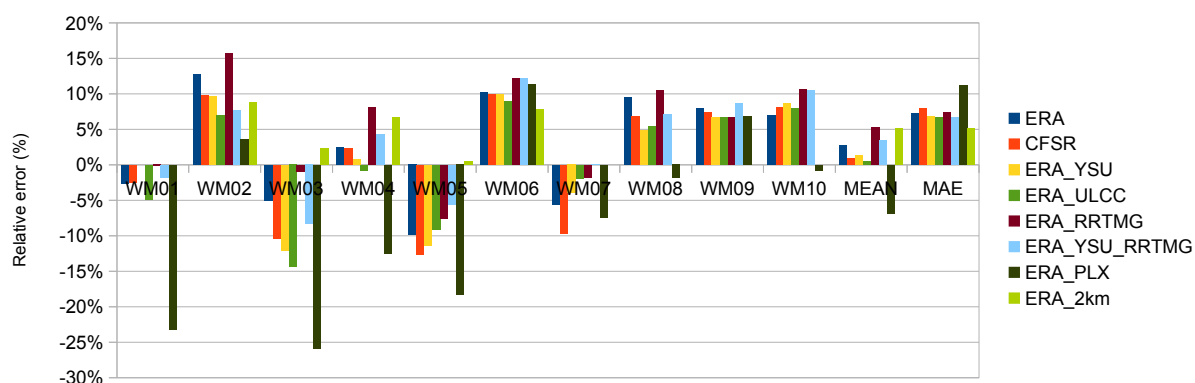
Figure 4.4 – Relative error ((WRF - OBS)/OBS in %) between the annual mean generalized wind from the observed wind atlas (OWA) and that for the numerical wind atlas (NWA) for a series of WRF sensitivity experiments in Table 4.1 for each of the 10 WASA sites. The last two bars show the mean error (MEAN) and mean absolute error (MAE) for all the 10 sites and 6 sites for the 2km simulation.

The summary of the relative errors in generalized wind speed at each of the WASA sites is presented in Fig. 4.4. From these we can conclude that for all the 5 km $\times$ 5 km experiments there is no clear combination of physical parameterizations that is superior to the others. However, the results from the ERA-PLX experiment are significantly worse than the others using the NOAA land surface model.

4.2   Generalization parameters

In addition to the WRF model setup, choices had to be made regarding the generalization method. In Table 4.3 we compare the mean generalized wind speed (h=100 m and z0=0.03 m) when using: stability corrections from WRF and standard values for A and B (M3) as described in section 2.2.3, neutral conditions and standard values for A and B (M4) as outlined at the end of section 2.2.3, as in (M3) but with new values of A and B as constants for all latitudes (M6), latitude-dependent A and B as linear functions of the sine of the latitude. These two later methods are described in section 2.3.

The various methods and parameters give quite different statistics concerning the mean generalized wind speed. Methods M4, M6 and M7 under predict the wind speed, while M3 slightly over predict it. The MAE of the mean generalized wind speed at M3 and M7 is very similar. We chose the M3 method for the remainder of the calculations because the statistics are slightly better, but further investigations could show M7 to be superior to M3. The observing periods are not quite the same as the simulated ones for WM04 and WM10. For these two sites the statistics are improved when using the actual observing periods when computing the generalized winds (see Table 5.2).

Table 4.3 – Summary statistics for the mean generalized wind speed for h=100 m and z0=0.03 m from the various generalization parameters and methods. The period is 1 October 2010 to 30 September 2013 for all sites in the NWA.

Mast	OBS Mean wind (m s^{-1})	M3 Mean wind (m s^{-1})	M3 % error	M4 Mean wind (m s^{-1})	M4 % error	M6 Mean wind (m s^{-1})	M6 % error	M7 Mean wind (m s^{-1})	M7 % error
WM01	6.83	6.73	−1.46	6.11	−10.54	6.11	−10.48	6.37	−6.81
WM02	6.68	7.31	9.43	7.06	5.69	6.55	−1.95	6.93	3.84
WM03	7.38	6.99	−5.28	6.60	−10.57	6.25	−15.38	6.63	−10.15
WM04	7.50	8.21	9.47	7.98	6.40	7.27	−3.06	7.77	3.47
WM05	8.98	9.08	1.11	8.62	−4.01	8.19	−8.87	8.68	−3.36
WM06	7.86	8.27	5.22	8.02	2.04	7.28	−7.40	7.67	−2.43
WM07	7.78	7.39	−5.01	6.69	−14.01	6.55	−15.77	7.01	−9.91
WM08	8.01	8.08	0.87	8.64	7.87	7.24	−9.68	7.95	−0.84
WM09	8.33	8.45	1.44	8.24	−1.08	7.48	−10.06	7.93	−4.77
WM10	7.12	7.73	8.57	7.65	7.44	6.81	−4.37	7.24	1.66
Mean Error			2.43		−1.08		−8.70		−2.93
MAE			4.79		6.96		8.70		4.72

4.3 Grid characteristics

In view of the large errors in the 5km simulations at masts WM02 and WM05 (Fig. 4.4) a new domain was selected and a 2 km × 2 km run was conducted for the same 13 month period. Because the domain is very large and thus computationally very expensive, only WM02–WM06 could be included in the domain of this simulation. The errors of this run (bright green bar) compared to those in the 5 km × 5 km experiments are also presented in Fig. 4.4. The relative error in wind generalized speed of this last simulation is much improved for most sites, except for WM04.

4.4 Recommendations from sensitivity studies

From the results from the sensitivity studies we can conclude that:

1. Once a domain configuration and horizontal grid spacing is selected, there is very little sensitivity to most physics options with respect to the annual mean wind speed at 100 m AGL. The errors from the various sensitivity experiments at the WASA sites vary very little from one experiment to the other.

2. There is large sensitivity to the choice of land surface scheme, both because of the land surface model itself, but also because of the different treatment of the surface roughness length. The NOAH land surface model uses a dominant vegetation for each model grid square, while the PLX scheme uses a multiple vegetation types, each with a different fraction, for each grid.

3. For some sites (e.g. WM02 and WM05) the use of high resolution ($\geq$ 3 km) reduces the errors is mean wind speed. The wind roses (not shown) also appear much improved by the use of high resolution.

4. The use of small high-resolution domains (not shown) did not improve the errors at WM02 and WM05.

These conclusions were fundamental in defining the final model WRF configuration used in the WASA NWA. The results of the large 3 km × 3 km domain (Table 5.2) are much improved from those presented in Fig. 4.4.

Chapter 5

Wind atlas validation

5.1 Wind climatologies

Table 5.1 compares the long-term averaged generalized wind speed for the observations and the model simulations using NWA derived from the KAMM simulations at all the WASA masts. The comparison is made between two periods: 1 October 2010 – 30 September 2012 and 1 October 2010 – 30 September 2013. The generalized wind mean wind speeds were derived using adapted parameters instead of the default mean heat flux over land. This effect is more pronounced at WM01 (heat flux of 40 $\mathrm{W\,m^{-2}}$) and WM10 (20 $\mathrm{W\,m^{-2}}$) compared to the default value of -40 $\mathrm{W\,m^{-2}}$ used in the standard WAsP.

Table 5.1 – Comparison of the mean generalized wind speed (h=100m and z0=0.03m) for all WASA masts for the observations ($\overline{U}_{OBS}$), and the KAMM-derived NWA ($\overline{U}_{KAMM}$) for different time periods (2 and 3 years). The $\overline{U}_{OBS}$ values are determined from the adapted wind profile as described in Table 16 of Mortensen et al. (2014b). The time periods are 2 years: 1 October 2010 – 30 September 2012; 3 years: 1 October 2010 – 30 September 2013 in the KAMM-derived values. Shorter time periods are used in the OBS values (for more details see Mortensen et al., 2014b) for WM04, WM09 and WM10.

Station	$\overline{U}_{OBS}$ 2 yrs ($\mathrm{m\,s^{-1}}$)	$\overline{U}_{KAMM}$ 2 yrs ($\mathrm{m\,s^{-1}}$)	$\overline{\Delta U}$ 2 yrs (%)	$\overline{U}_{OBS}$ 3 yrs ($\mathrm{m\,s^{-1}}$)	$\overline{U}_{KAMM}$ 3 yrs ($\mathrm{m\,s^{-1}}$)	$\overline{\Delta U}$ 3 yrs (%)
WM01	6.34	5.38	-15.1	6.40	5.53	-13.6
WM02	6.50	6.90	6.2	6.55	7.03	7.3
WM03	7.19	6.62	-7.9	7.25	6.70	-7.6
WM04	7.39	6.99	-5.4	7.44	7.16	-3.8
WM05	9.00	8.49	-4.9	9.05	8.59	-5.1
WM06	7.55	7.20	-4.6	7.73	7.33	-5.2
WM07	7.48	6.63	-11.4	7.56	6.69	-11.5
WM08	7.72	7.64	-1.0	7.72	7.61	-1.4
WM09	7.72	7.44	-3.6	8.05	7.41	-7.9
WM10	6.32	6.04	-4.4	6.86	6.14	-10.5
Mean error			-5.2			-5.9
Mean absolute error (MAE)			6.5			7.4

Table 5.2 compares the long-term (3 years) averaged generalized wind speed for the observations and the model simulations using NWA derived from KAMM and WRF at all the WASA masts. The winds correspond to a height of 100 m AGL and a roughness of 0.03 m. The mean wind is derived from the parameters in the WAsP lib file as described in section 2.2. Most OWA are for the period 1 October 2010 – 30 September 2013, except for WM04, WM08-WM10 that contain some missing data (for more details see Mortensen et al., 2014a).

Table 5.2 – Comparison of the mean generalized wind speed (h=100m and z0=0.03m) for all WASA masts for the observations ($\overline{U}_{OBS}$), and the NWA from KAMM ($\overline{U}_{KAMM}$) and WRF ($\overline{U}_{WRF}$). In the KAMM-derived NWA values the period is 1 October 2010 – 30 September 2013 for all sites. In the WRF-derived NWA values, the time period is 1 October 2010 – 30 September 2013 for most sites, but 1 June 2010 to 31 May 2013 for WM04; 1 March 2011 to 28 February 2012 and 1 October 2012 to 30 September 2013 for WM10. $\overline{U}_{OBS}$ has been derived using default (-40 W m^{-2}) mean heat flux over land.

Station	$\overline{U}_{OBS}$ (m s^{-1})	$\overline{U}_{KAMM}$ (m s^{-1})	$\overline{\Delta U}_{KAMM-OBS}$ (%)	$\overline{U}_{WRF}$ (m s^{-1})	$\overline{\Delta U}_{WRF-OBS}$ (%)
WM01	6.83	5.53	-19.03	6.73	-1.46
WM02	6.68	7.03	5.24	7.31	9.43
WM03	7.38	6.70	-9.21	6.99	-5.28
WM04	7.50	7.16	-4.53	8.15	8.67
WM05	8.98	8.59	-4.34	9.08	1.11
WM06	7.86	7.33	-6.74	8.27	5.22
WM07	7.78	6.69	-14.01	7.39	-5.01
WM08	8.01	7.61	-4.99	8.08	0.87
WM09	8.33	7.41	-11.04	8.45	1.44
WM10	7.12	6.14	-13.76	7.53	5.69
Mean error			-8.24		2.46
Mean absolute error (MAE)			9.29		4.75

The biases between generalized wind derived from OWA (Mortensen et al., 2014b) and NWA vary greatly with model and site. Overall, the KAMM-derived mean generalized winds are underestimated for most sites except for WM02. The sites where thermal-induced flows are important in determining the wind climate (e.g. WM01, WM03) are the most affected. In the WRF-derived NWA, biases are mostly positive, except for WM01, WM03, and WM06, but the absolute value of all biases is smaller than 10%. At two of the sites, WM02 and WM10, the bias is quite large, and probably attributable to overestimation of winds under stable conditions.

Figures 5.1 to 5.10 compare the wind climatologies from the observed wind atlas (OWA) and numerical wind atlas (NWA) derived from the winds in the KAMM and WRF simulations for all 10 sites. The comparison is in the form of wind roses drawn from the generalized wind climate files. In each of the panels, the figure on the left is the frequency of wind sector, the figure on the right is the wind speed distribution for each sector (gray lines) and the combined from all sectors (dark solid is the emergent and the dash is the combined frequency distribution).

5.1.1 Alexander Bay (WM01)

The observed and simulated generalized wind climate at WM01 are shown in Fig. 5.1. The wind rose is very well simulated by the WRF-derived NWA, with southerly- to southeasterly-dominated flow. The KAMM-based NWA wind rose (Fig. 5.1a) shows an almost dominance of southerly flow and the annual mean generalized wind speed is severely underestimated.

(a) KAMM/WAsP   **(b)** WRF

(c) Observation

Figure 5.1 – Graphical representation of the WAsP wind climate files ("lib") at WM01 for the period 1 October 2010 to 30 September 2013. The generalized wind climates are for h=100 m and z0=0.03 m. The OWA uses default heat fluxes.

5.1.2 Clavinia (WM02)

The observed and simulated wind atlas for WM02 are shown in Fig. 5.2. In the OWA, the wind rose shows flow from most sectors, with a small maximum from the SSE. The wind rose derived from the WRF NWA displays other small maxima from other sectors (E and NE). These are probably consequences of poor representation of the terrain upstream from the site.

(a) KAMM/WAsP   **(b)** WRF

(c) Observation

Figure 5.2 – Graphical representation of the WAsP wind climate files ("lib") at WM02 for the period 1 October 2010 to 30 September 2013. The generalized wind climates are for h=100 m and z0=0.03 m. The OWA uses default heat fluxes.

5.1.3 Vredendal (WM03)

The graphical representation of the OWA and NWA for WM03 is presented in Fig. 5.3. Here there is excellent correspondence between the OWA and the WRF-derived NWA. The wind rose is dominated by flow from the S–SW, with a secondary maximum from the NE–E.

File = SA5050_m7_p201010_201309WM03.4_5.lib
z0 = 0.03 m   h= 100 m

File = wrf_WASA_3_N_31.746S_18.414E.lib
z0 = 0.03 m   h= 100 m

(a) KAMM/WAsP   **(b)** WRF

File = WM03.lib
z0 = 0.03 m   h= 100 m

(c) Observation

Figure 5.3 – Graphical representation of the WAsP wind climate files ("lib") at WM03 for the period 1 October 2010 to 30 September 2013. The generalized wind climates are for h=100 m and z0=0.03 m.

5.1.4 Vredenburg (WM04)

For WM04 the OWA and NWAs are graphically represented in Fig. 5.4. The OWA-derived wind rose shows flow dominated by the SW–S sector. In the WRF-derived NWA, the rose is "rotated" counterclockwise with maximum frequencies from the S. A secondary maximum from the North is well simulated in the WRF-derived NWA.

(a) KAMM/WAsP

(b) WRF

(c) Observation
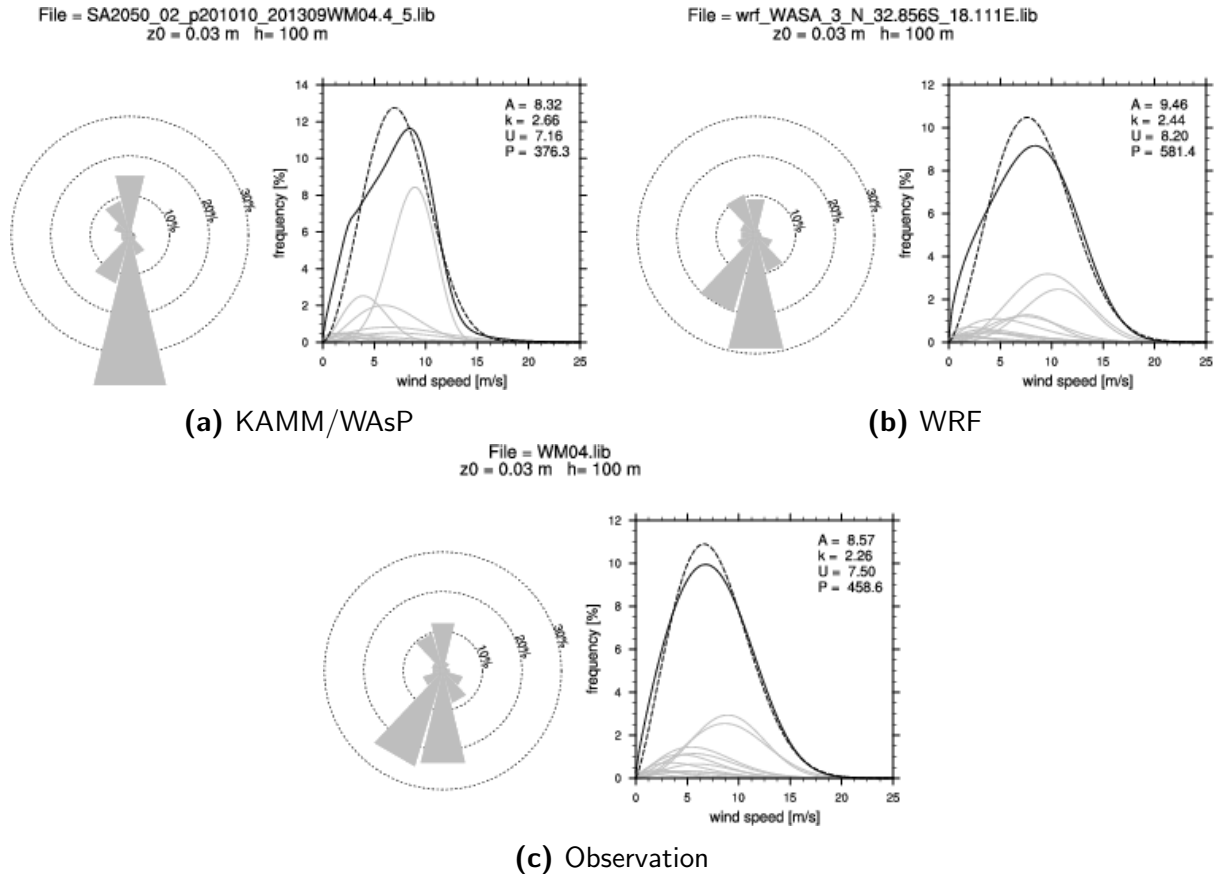
Figure 5.4 – Graphical representation of the WAsP wind climate files ("lib") at WM04 for the period 1 June 2010 to 31 May 2013 (1 October 2010 to 30 September 2013 for KAMM-derived NWA). The generalized wind climates are for h=100 m and z0=0.03 m. The OWA uses default heat fluxes.

5.1.5 Napier (WM05)

The graphical representation of the wind atlas for WM05 is presented in Fig. 5.5. As opposed to the sites to the North (WM01–WM04), the flow here is either from the West or the East following the large-scale atmospheric conditions. Under these conditions, both KAMM and WRF NWA compare well with the observations.

File = SA2050_02_p201010_201309WM05.4_5.lib
z0 = 0.03 m   h= 100 m

File = wrf_WASA_3_N_34.609S_19.676E.lib
z0 = 0.03 m   h= 100 m

(a) KAMM/WAsP   **(b)** WRF

File = WM05.lib
z0 = 0.03 m   h= 100 m

(c) Observation
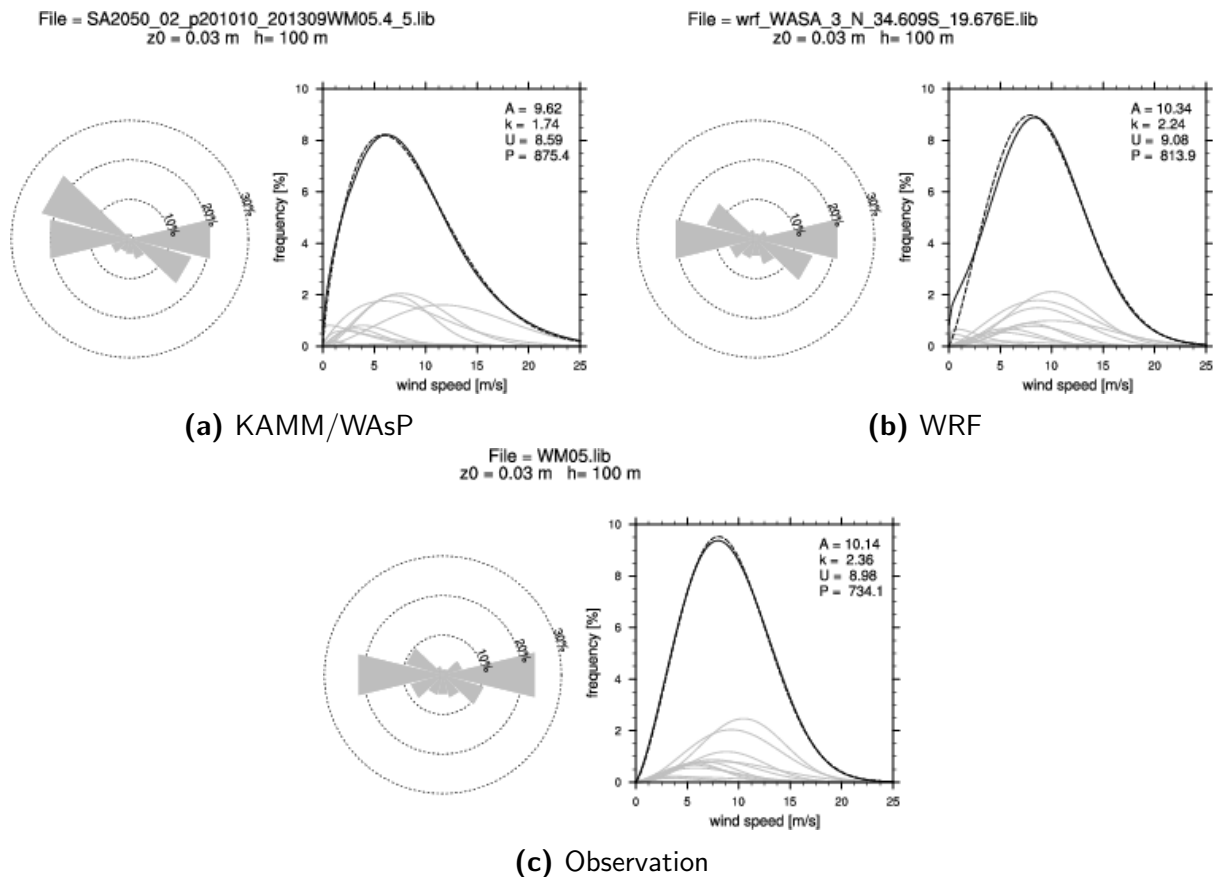
Figure 5.5 – Graphical representation of the WAsP wind climate files ("lib") at WM05 for the period 1 October 2010 to 30 September 2013. The generalized wind climates are for h=100 m and z0=0.03 m. The OWA uses default heat fluxes.

5.1.6 Sutherland (WM06)

At Sutherland (WM06, Fig. 5.6) the wind climate is also dominated by the W and E components (Fig. 5.6c). Both the KAMM- and WRF-based NWA represent well this behavior with a slight overestimation of the frequencies from the NW sector. This site is located a few kilometers NE from the escarpment and thus is not unexpected that the mesoscale models have difficulties in simulating the details of the flow.

(a) KAMM/WAsP   **(b)** WRF

(c) Observation
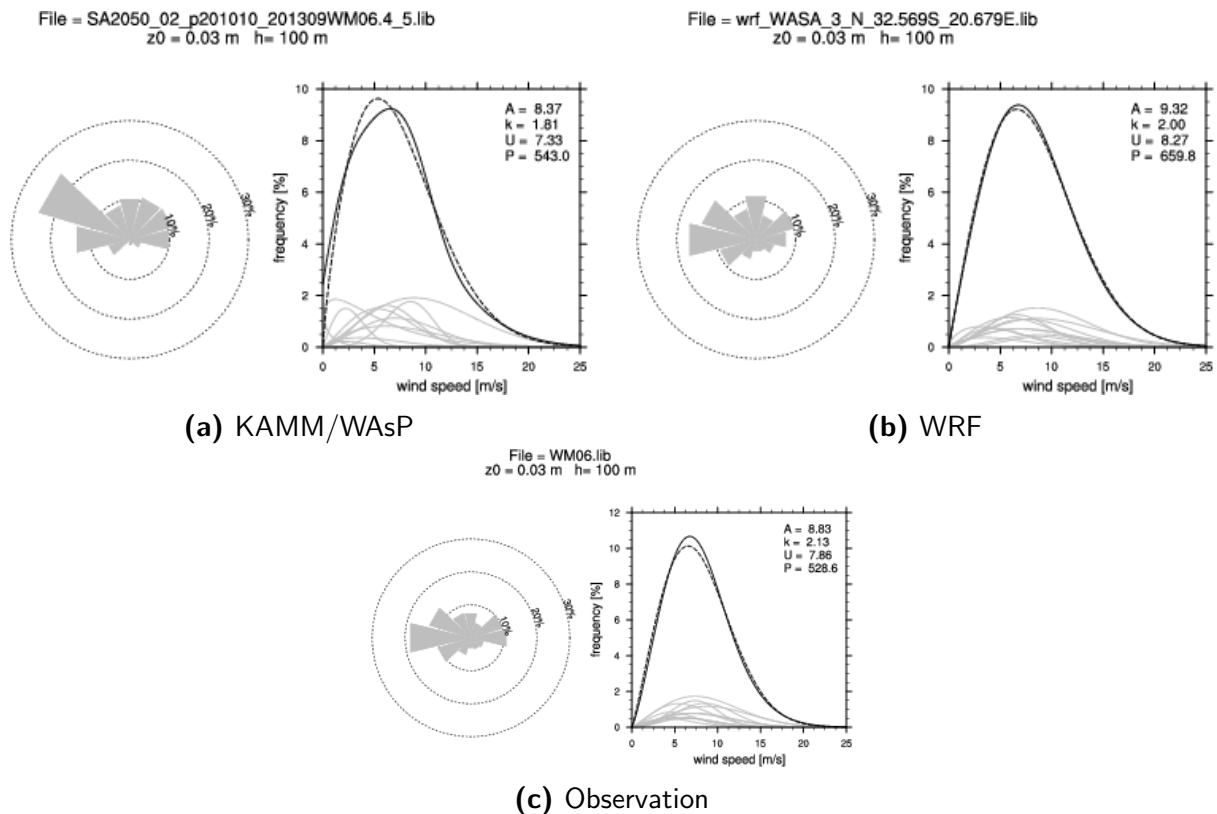
Figure 5.6 – Graphical representation of the WAsP wind climate files ("lib") at WM06 for the period 1 October 2010 to 30 September 2013. The generalized wind climates are for h=100 m and z0=0.03 m. The OWA uses default heat fluxes.

5.1.7 Beaufort West (WM07)

The OWA and NWAs at WM07 are graphically presented in Fig. 5.7. As in WM05 and WM06, the frequencies in the wind rose are dominated by the W and E sectors, and both NWAs capture well this behavior. However, the magnitude of the mean annual generalized wind is underestimated by the two methods.

(a) KAMM/WAsP   **(b)** WRF

(c) Observation
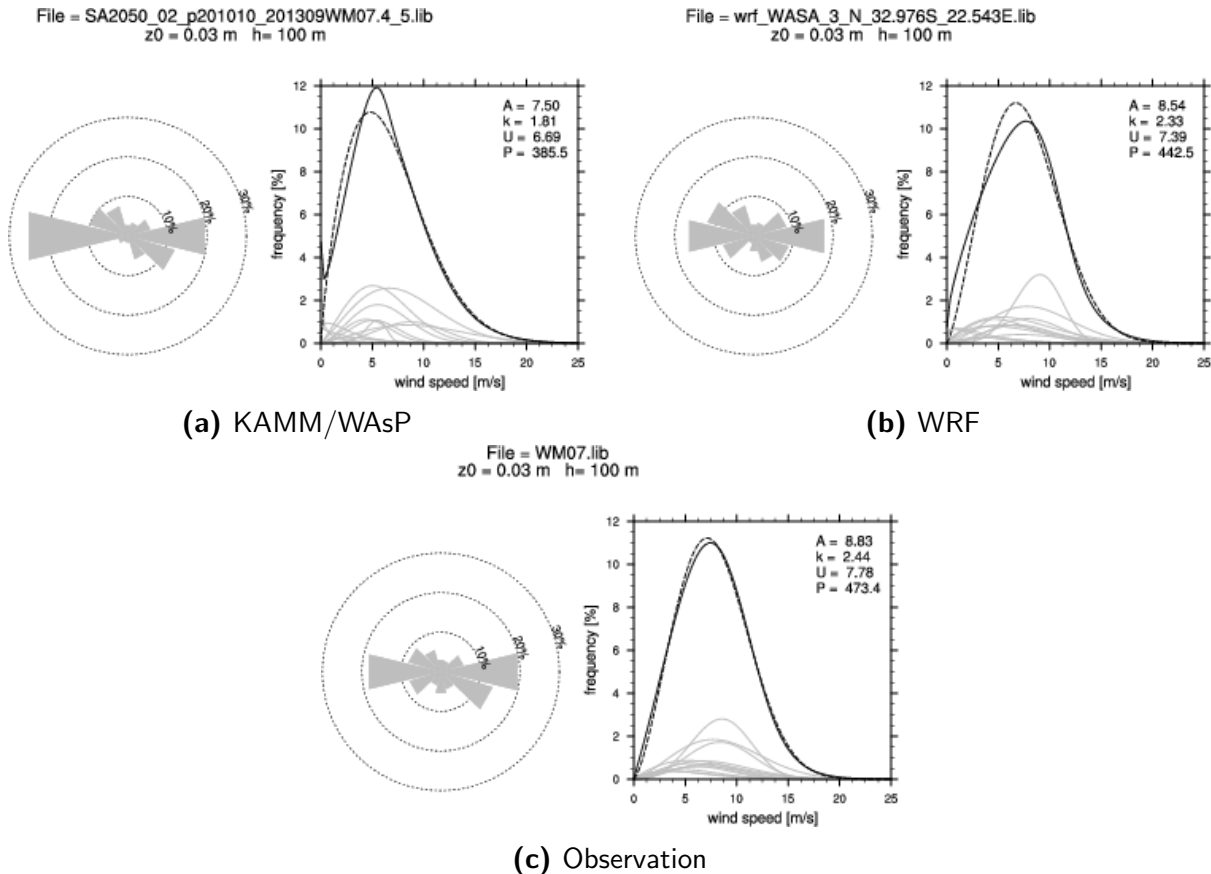
Figure 5.7 – Graphical representation of the WAsP wind climate files ("lib") at WM07 for the period 1 October 2010 to 30 September 2013. The generalized wind climates are for h=100 m and z0=0.03 m. The OWA uses default heat fluxes.

5.1.8 Humansdorp (WM08)

The wind climate at WM08 as seen in the OWA and NWAs is presented in Fig. 5.8. This is the southernmost WASA mast and is located close to the south coast. As in WM05 the wind rose is dominated by W and E flow, which is well characterized by both NWAs. The magnitude of the mean generalized wind is overestimated by the WRF-based NWA and underestimated by the KAMM-based NWA.

(a) KAMM/WAsP   **(b)** WRF
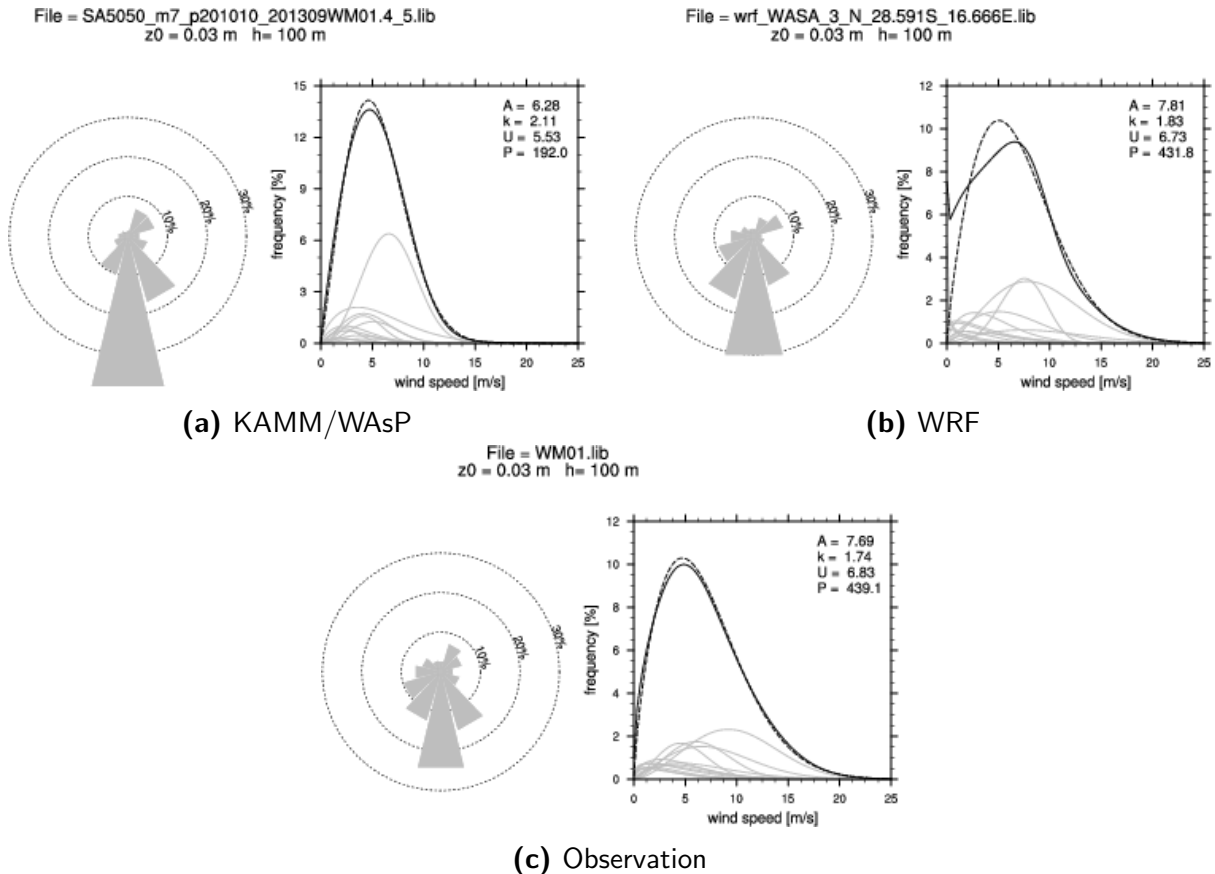

(c) Observation
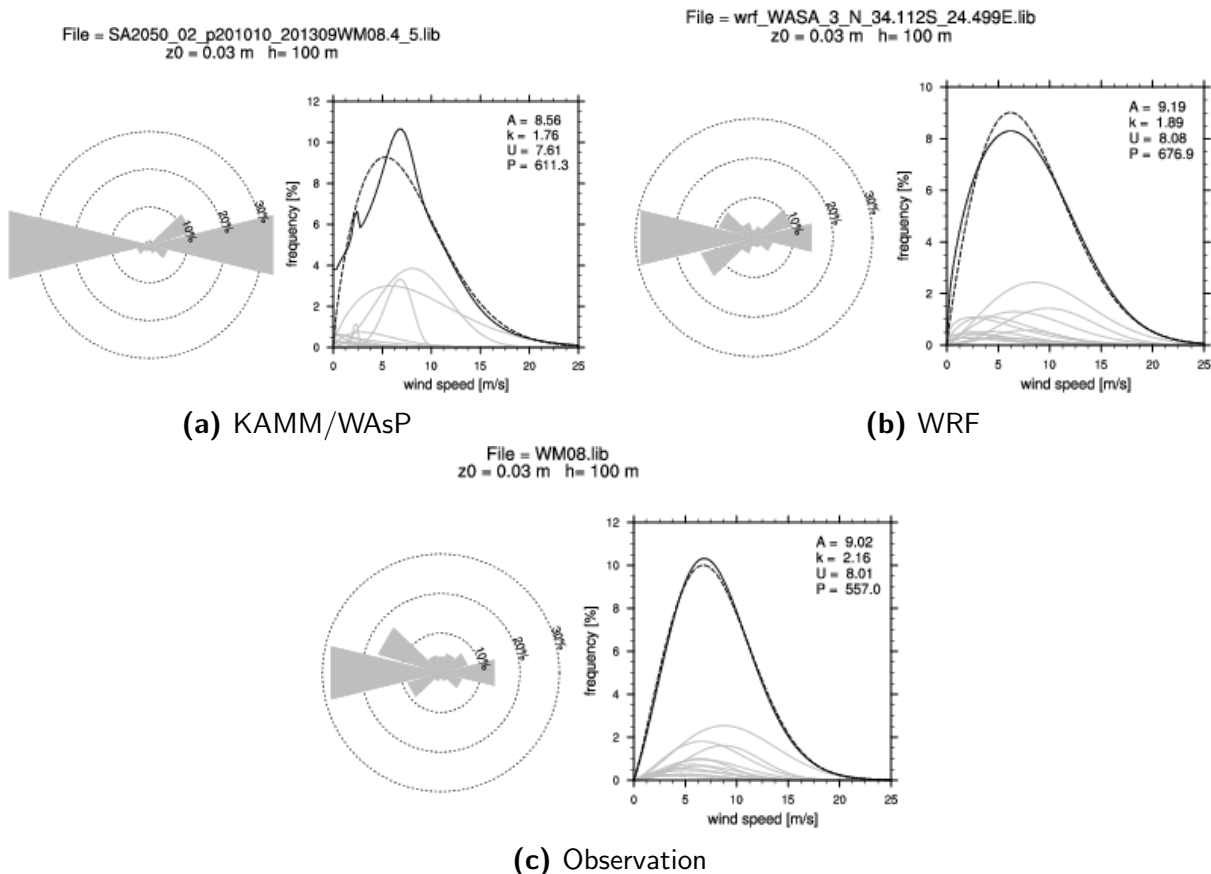
Figure 5.8 – Graphical representation of the WAsP wind climate files ("lib") at WM08 for the period 1 October 2010 to 30 September 2013. The generalized wind climates are for h=100 m and z0=0.03 m. The OWA uses default heat fluxes.

5.1.9 Noupoort (WM09)

Figure 5.9 presents the generalized wind climate at WM09 in the observations and the model-based NWA. The flow at this site is dominated by the NW sector and this is well captured by both NWAs. As with other sites, the WFR-based NWA overestimates the mean generalized wind, while the KAMM-based NWA underestimates it.

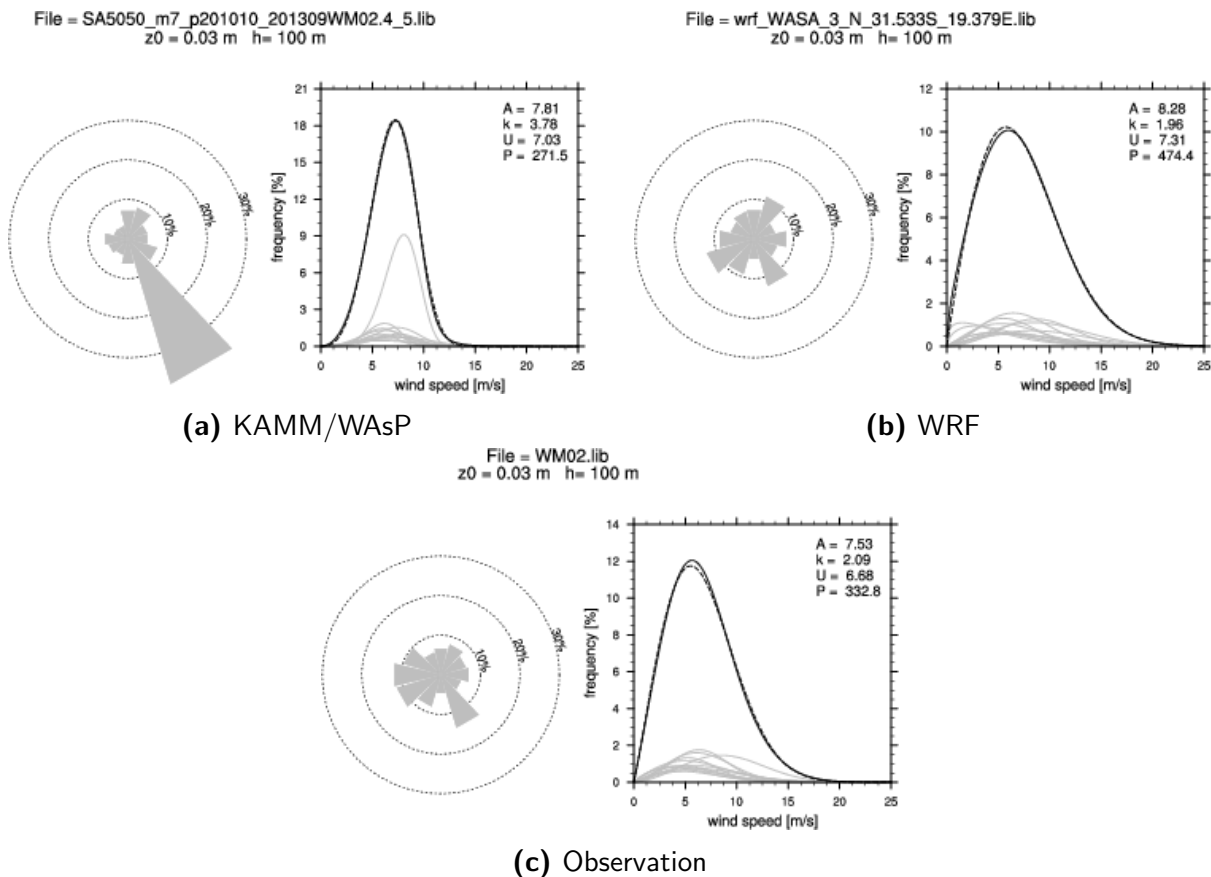**(a)** KAMM/WAsP   **(b)** WRF
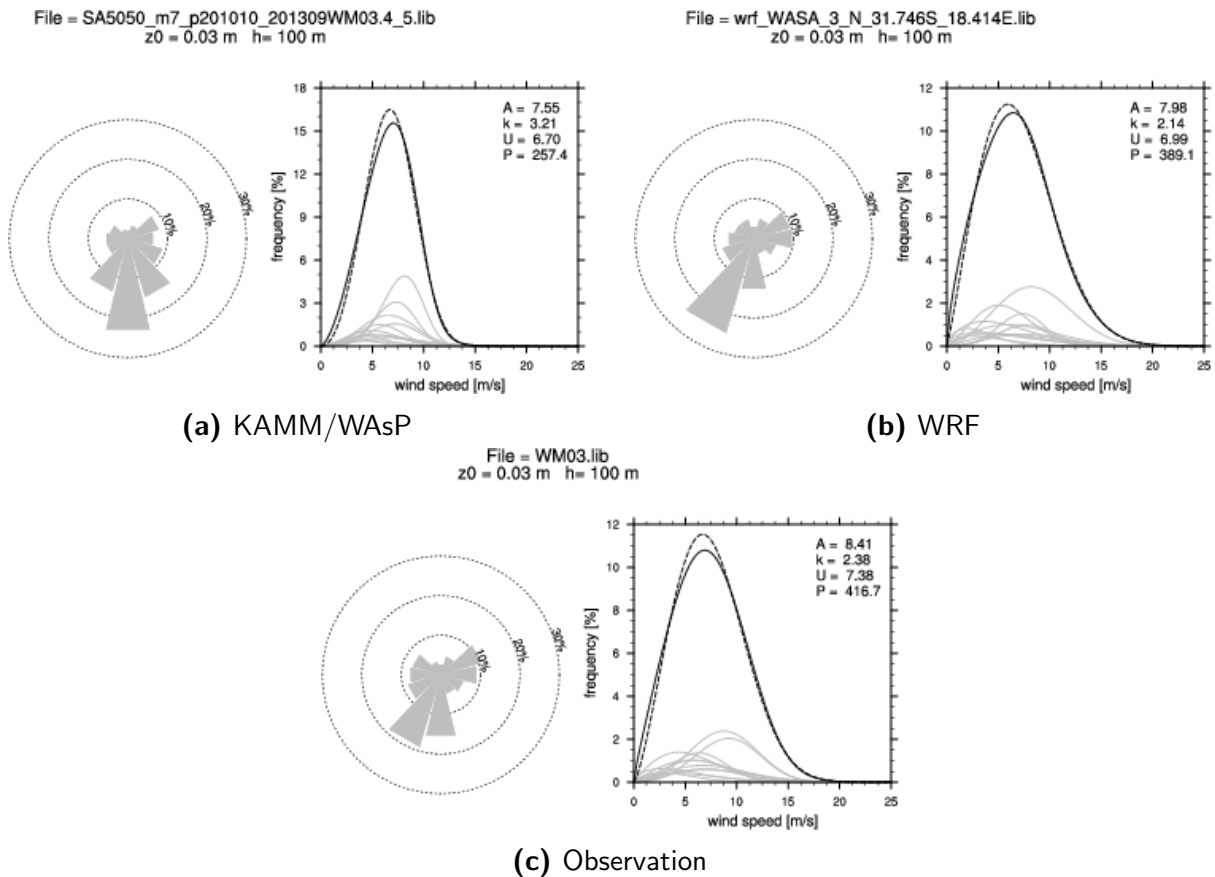
(c) Observation
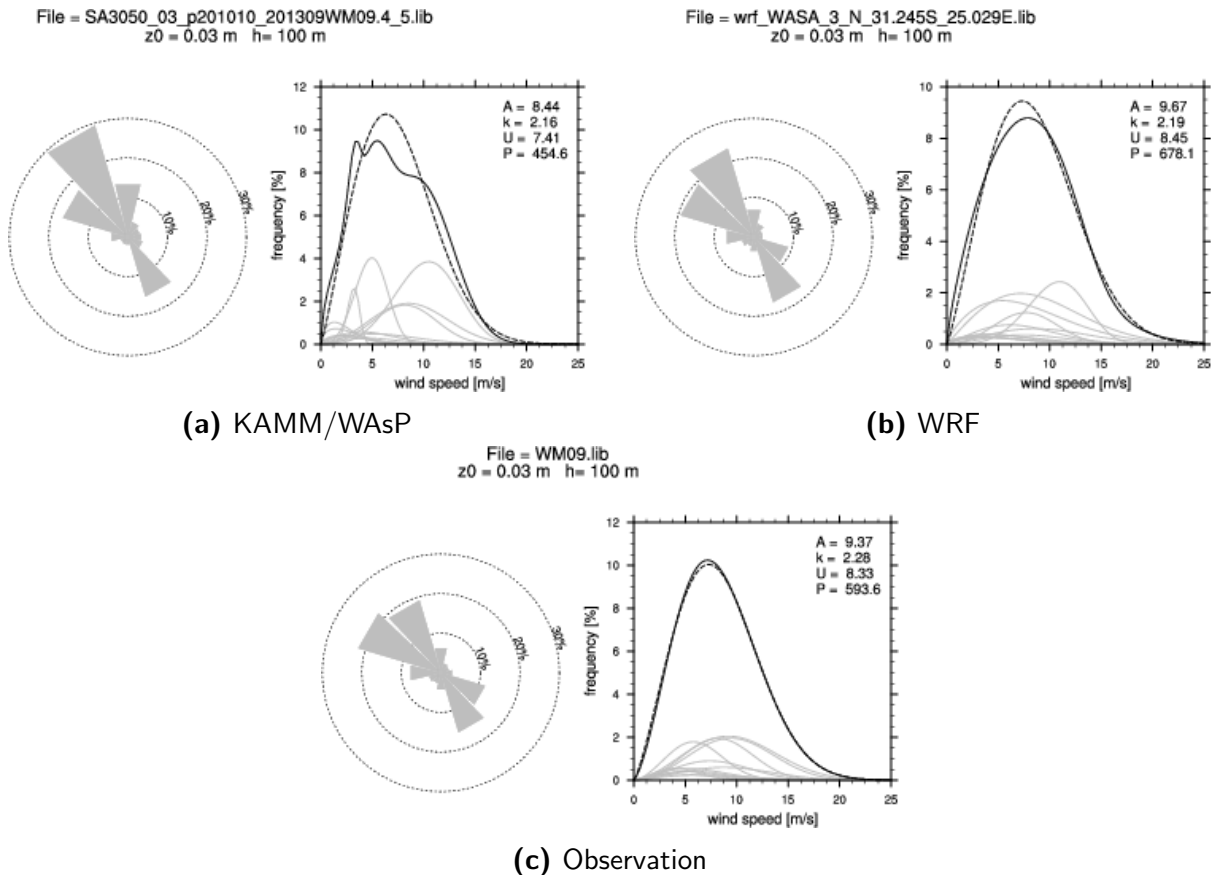
Figure 5.9 – Graphical representation of the WAsP wind climate files ("lib") at WM09 for the period 1 October 2010 to 30 September 2013 in the NWA. The OWA is for the 2-y period, consisting of data from October 2010 to September 2013 — less the calendar year 2011. The generalized wind climates are for h=100 m and z0=0.03 m. The OWA uses default heat fluxes.

5.1.10 Butterworth (WM10)

The graphical representation of the wind climate at WM10 is shown in Fig. 5.10. Interestingly the observed generalized wind rose at this site shows no preferential sector and the averaged mean wind is relatively low. Evidence from the microscale modeling (Report XX) and the wind shear climatology in Fig. 2.4, the stability at this site is often unstable. This can help explain the low estimate in the KAMM-based NWA. In the WRF-based NWA, the mean generalized wind is overestimated, but the Weibull distributions for each individual sector are well represented.

(a) KAMM/WAsP   **(b)** WRF

(c) Observation
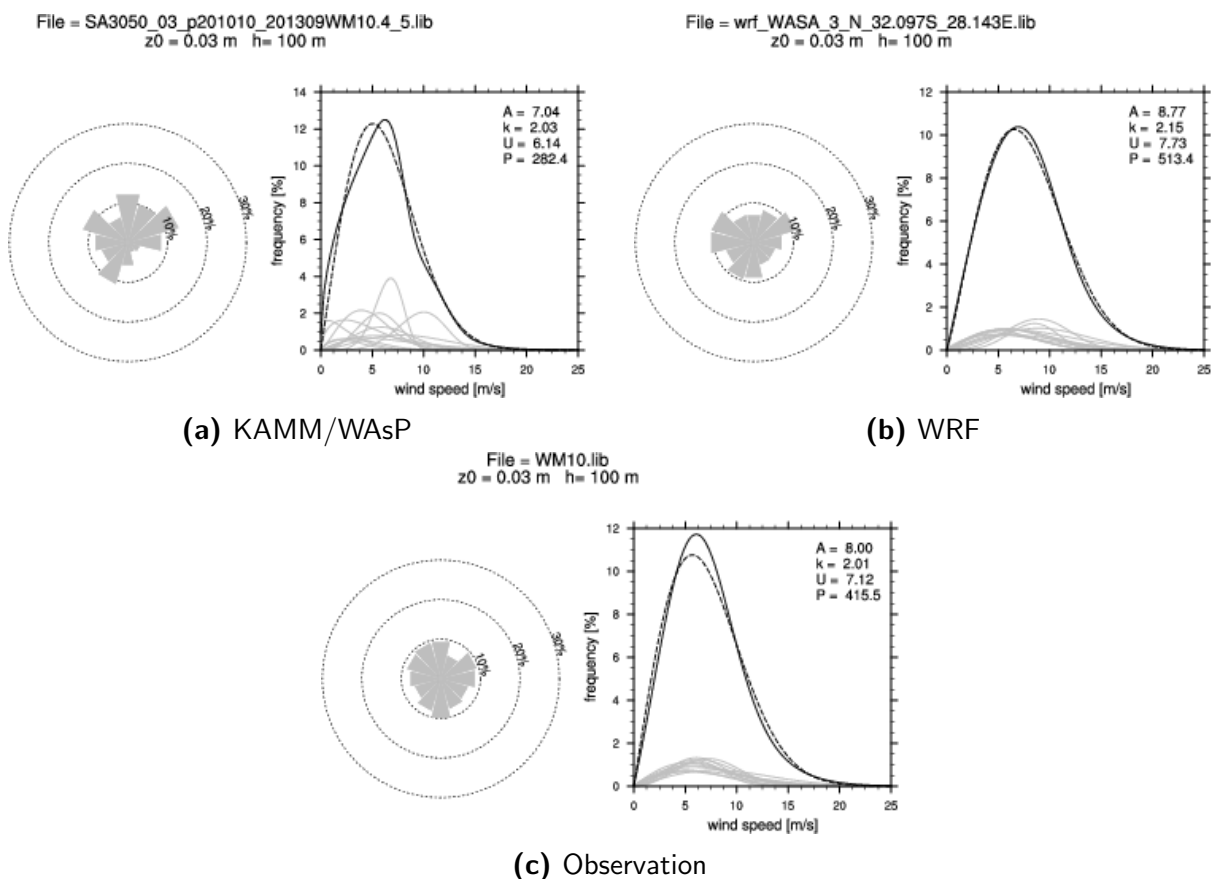
Figure 5.10 – Graphical representation of the WAsP wind climate files ("lib") at WM10 for the period 1 March 2011 to February 2012 and October 2012 to September 2013. The KAMM-derived NWA is for the period 1 October 2010 to 30 September 2013. The generalized wind climates are for h=100 m and z0=0.03 m. The OWA uses default heat fluxes.

5.2 Seasonal and diurnal cycles

The WRF regional model provides wind data that is time synchronous with data from the 10 WASA wind measurement masts erected as part of the project. The period of overlap is three years for most masts although in some masts there is missing data. A validation of the WRF wind output is carried out at each of the 10 WASA measurement masts for wind speeds at 62 m A.G.L. The diurnal and annual cycle of wind speed at each mast is compared with data from each respective WRF-based grid cell in which the mast would be situated. For each of the 10 masts the following assessments were made:

1. Histogram of wind speed

2. Seasonal cycle

3. Diurnal cycle

4. Summary statistics (mean bias, root mean squared error (RMSE), mean absolute cycle bias, which is the mean absolute difference between the diurnal cycles across the seasonal cycle, and a Pearson's correlation coefficient).

The summary statistics are presented in Table 5.3 for the 10 masts. Biases are quite low and vary from $-0.65 \mathrm{m\,s^{-1}}$ at WM05 to $0.47 \mathrm{m\,s^{-1}}$ at WM02. At 4 of the masts the absolute value of the mean bias is lower than $0.1 \mathrm{m\,s^{-1}}$. RMSE are lower than $2.7 \mathrm{m\,s^{-1}}$ at all masts. The Pearson's correlation coefficients are in the range of 0.72–0.86 for the hourly data, 0.82–0.93 for the daily values and 0.78–0.97 for the monthly data.

Table 5.3 – Summary statistics at the 10 mast sites. The mean bias, RMSE and mean absolute cycle bias are calculated using hourly data. The Pearson correlation is calculated using hourly, daily and monthly wind speed averages.

Mast	Mean Bias $(\mathrm{m\,s^{-1}})$	RMSE $(\mathrm{m\,s^{-1}})$	Mean absolute cycle bias $(\mathrm{m\,s^{-1}})$	Pearson correlation coefficient		
				hourly	daily	monthly
WM01	−0.04	2.4	0.46	0.78	0.82	0.87
WM02	0.47	2.5	0.61	0.74	0.87	0.88
WM03	−0.46	2.1	0.52	0.78	0.85	0.90
WM04	0.04	1.9	0.48	0.83	0.93	0.97
WM05	−0.65	2.2	0.66	0.86	0.93	0.89
WM06	0.45	2.3	0.55	0.79	0.92	0.91
WM07	−0.14	2.3	0.38	0.72	0.86	0.78
WM08	−0.08	2.5	0.47	0.76	0.89	0.86
WM09	0.42	2.4	0.45	0.84	0.91	0.97
WM10	−0.02	2.7	0.66	0.74	0.83	0.89

Mast data is compared with values of the corresponding model grid cell the mast would be in. For each mast-grid cell comparison we analyze the histogram of wind speed frequency, the mean seasonal cycle, mean diurnal cycle and monthly wind speed averages (top panel in Figs. 5.11–5.20). Furthermore, for each month of the 3-year period, average wind speeds

are computed for each hour of the 24-hour day to assess the diurnal cycle at a monthly and annual scale (bottom panel in Figs. 5.11–5.20). In this panel the mast data averaged over the full observation period are in the left-hand column and corresponding WRF grid cell data in the right-hand column.

At some of the masts there are periods for which there is no data. Masts affected are WM02, WM04, WM07, WM08, WM09 and WM10. Missing data were excluded in assessments except in the month-by-month record where these data gaps are apparent.

For each mast the observed wind climate is briefly presented and then compared against the model results. The referred to in the text are austral summer (December, January, February), autumn (March, April, May), winter (June, July, August) and spring (September, October, November).

5.2.1 Alexander Bay (WM01)

At WM01 (Fig. 5.11), wind speeds are highest in the afternoon and early evening during the austral summer months. The WRF model captures the shape of the mean seasonal cycle very well with only a small over-simulation (under-simulation) of wind speeds in June and July (August to December). The model also captures the shape of the diurnal cycle of wind speed extremely well with only a slight under-simulation of wind speeds in the late afternoon. There is a slight phase error in the peak of the maximum wind speed from around 16:00 in the observations to 18:00 in the WRF simulations. The model slightly underestimates the frequency of wind speeds between 2–4 m s^{-1} with a corresponding slight overestimation if wind speeds in the 5–7 m s^{-1} range.

Figure 5.11 – Comparison of the wind speed (m s^{-1}) at 62 m AGL at WM01: Wind speed distribution (top left), mean seasonal cycle (top center) and mean diurnal cycle (top right) in the mast measurements (blue) and in the WRF model simulations (green). Mean wind speed (m s^{-1}) at 62 m AGL as a function of the time of the day (x-axis) and the month of the year (y-axis) for the mast observations (bottom left) and the WRF simulations (bottom right).

5.2.2 Calvinia (WM02)

At WM02 (Fig. 5.12), the highest wind speeds are recorded in the afternoon and evening of the austral spring and summer. The WRF model generally over-simulates higher wind speeds at this site as evidenced in the histogram, the mean seasonal cycle and monthly averages. The diurnal cycle indicates much of this is the over-simulation of late night and early morning high wind speeds, although the shape of the diurnal cycle is still well captured.

There are missing data at this mast: December 2012, February 2013 and missing January 2013.

Figure 5.12 – Comparison of the wind speed $(m\,s^{-1})$ at 62 m AGL at WM02: Wind speed distribution (top left), mean seasonal cycle (top center) and mean diurnal cycle (top right) in the mast measurements (blue) and in the WRF model simulations (green). Mean wind speed $(m\,s^{-1})$ at 62 m AGL as a function of the time of the day (x-axis) and the month of the year (y-axis) for the mast observations (bottom left) and the WRF simulations (bottom right).

5.2.3 Vredendal (WM03)

The observations indicate highest wind speeds during the austral spring and summer in late in the afternoon. There is a general under-simulation of wind speeds during these months by the model but during austral winter differences are small. The model captures the shape of the diurnal cycle, however, it over-simulates morning wind speeds and under-simulates the high wind speeds in late afternoon and evening. The model over-simulates wind speeds between 5–8 m s^{-1} and under-simulates the frequency of wind speeds greater than 8 m s^{-1}.

Under-simulation of high afternoon winds leads to general under-simulation. The model does not capture well very high wind speeds of between 10–12 m s^{-1}.

Figure 5.13 – Comparison of the wind speed (m s^{-1}) at 62 m AGL at WM03: Wind speed distribution (top left), mean seasonal cycle (top center) and mean diurnal cycle (top right) in the mast measurements (blue) and in the WRF model simulations (green). Mean wind speed (m s^{-1}) at 62 m AGL as a function of the time of the day (x-axis) and the month of the year (y-axis) for the mast observations (bottom left) and the WRF simulations (bottom right).

5.2.4 Vredenburg (WM04)

Highest wind speeds at this mast (Fig. 5.14) are in the late austral spring and summer during the late afternoon and evening. The model over-simulates the frequency of wind speeds between 6–10 m s^{-1} but under-simulates wind speeds higher than 10 m s^{-1}. The seasonal cycle of wind speed is well captured except in May where the model over-simulates wind speeds. The shape of the diurnal cycle is again well captured but morning wind speeds are over-simulated and afternoon and evening wind speeds are under-simulated.

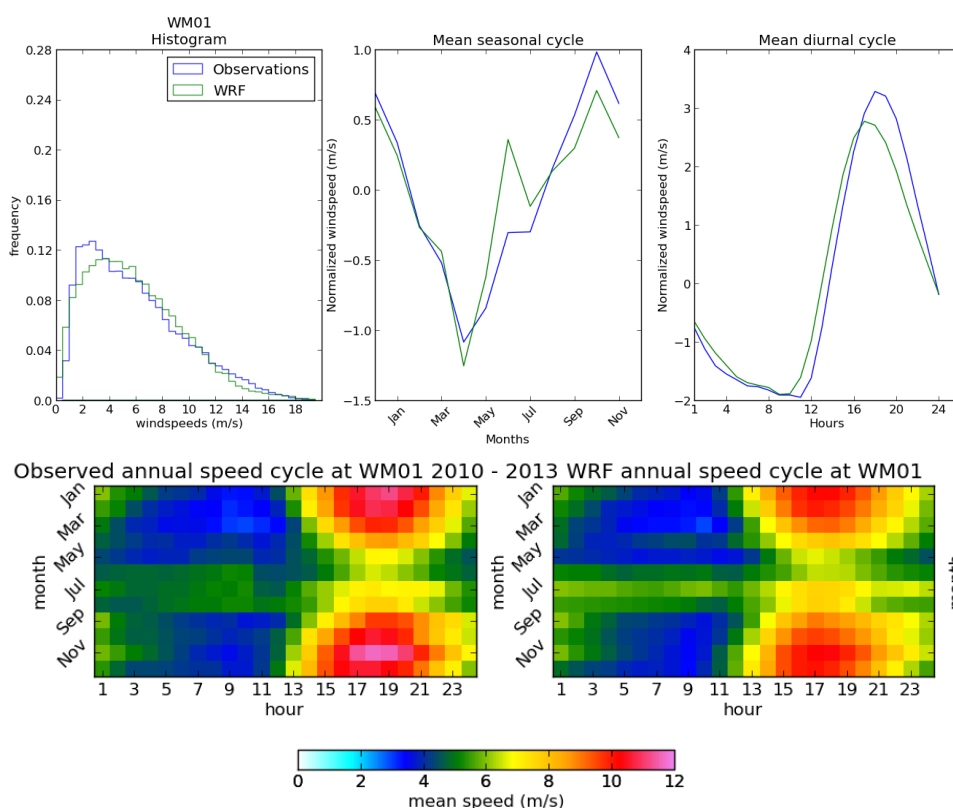There are missing data at this station: June 2013.

Figure 5.14 – Comparison of the wind speed (m s^{-1}) at 62 m AGL at WM04: Wind speed distribution (top left), mean seasonal cycle (top center) and mean diurnal cycle (top right) in the mast measurements (blue) and in the WRF model simulations (green). Mean wind speed (m s^{-1}) at 62 m AGL as a function of the time of the day (x-axis) and the month of the year (y-axis) for the mast observations (bottom left) and the WRF simulations (bottom right).

5.2.5 Napier (WM05)

Highest wind speeds at this mast are in the austral spring and summer during the early afternoon to early evening. The model generally under-simulates the wind speed in austral summer and over-simulates wind speed in austral winter but simulates the shape and magnitudes of the diurnal cycle very well.

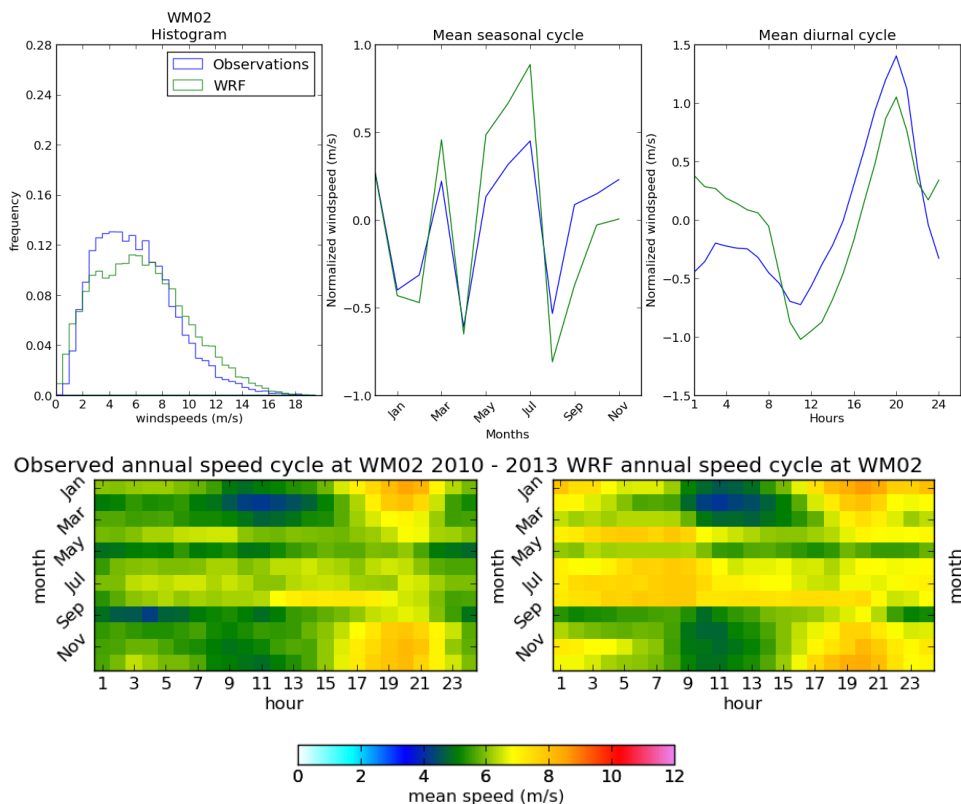There are missing data at this station: June 2011, September 2013.

Figure 5.15 – Comparison of the wind speed $(m\,s^{-1})$ at 62 m AGL at WM05: Wind speed distribution (top left), mean seasonal cycle (top center) and mean diurnal cycle (top right) in the mast measurements (blue) and in the WRF model simulations (green). Mean wind speed $(m\,s^{-1})$ at 62 m AGL as a function of the time of the day (x-axis) and the month of the year (y-axis) for the mast observations (bottom left) and the WRF simulations (bottom right).

5.2.6   Sutherland (WM06)

Highest wind speeds recorded at this mast are in austral winter with peaks in May and July. The diurnal cycle varies seasonally – during austral winter there is no clear time of day that records consistently higher wind speeds. During austral summer wind speeds in the afternoon are generally higher than in the morning. The model generally over-simulates the frequency of higher wind speeds (8–12 m s^{-1}) and under-simulates the frequency of wind speeds between 4–8 m s^{-1}). A general over-simulation of wind speeds is evident in the seasonal cycle, which in the diurnal cycle can be seen as an over-simulation of wind speeds in the morning in all seasons except summer as well as late night wind speeds generally. Although the shape of the diurnal cycle is very well captured by the model simulation, it is about 3 hours out of phase with the observations.
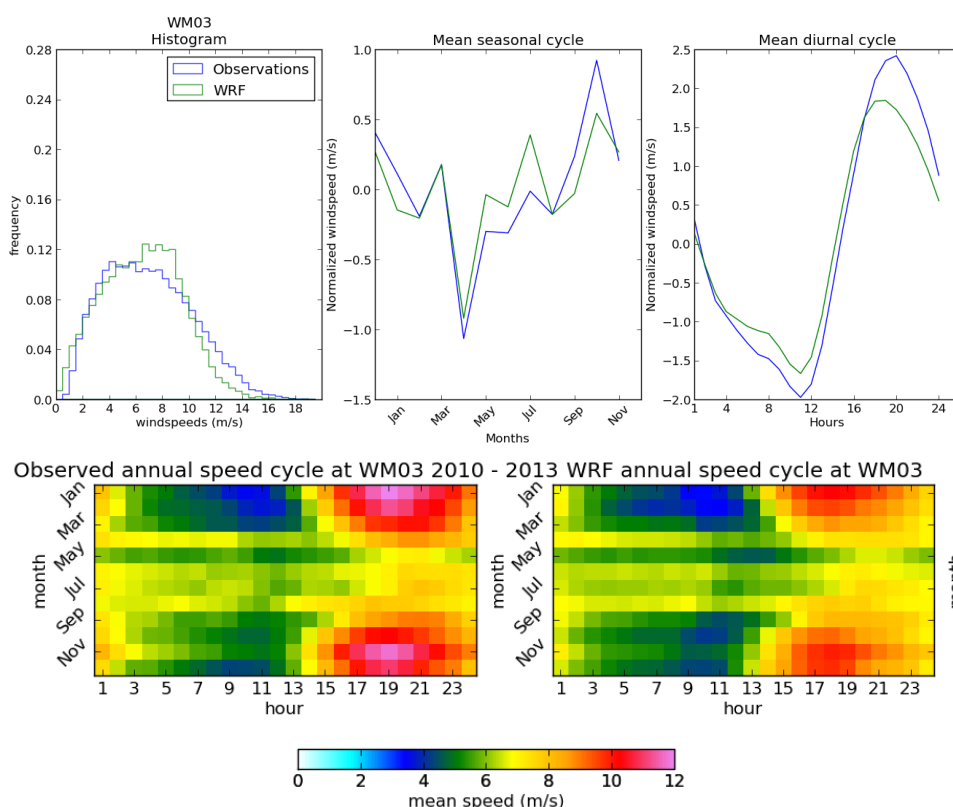

Figure 5.16 – Comparison of the wind speed (m s^{-1}) at 62 m AGL at WM06: Wind speed distribution (top left), mean seasonal cycle (top center) and mean diurnal cycle (top right) in the mast measurements (blue) and in the WRF model simulations (green). Mean wind speed (m s^{-1}) at 62 m AGL as a function of the time of the day (x-axis) and the month of the year (y-axis) for the mast observations (bottom left) and the WRF simulations (bottom right).

5.2.7   Beaufort West (WM07)

Highest wind speeds at this mast are in the late evening to early morning in the austral summer months with generally low wind speeds in the austral winter. The model over-simulates winter wind speeds but simulates slower wind speeds in the austral spring and summer seasons that leads to a small negative mean bias. The shape of the diurnal cycle is very well simulated.

There are missing data at this station: May 2013
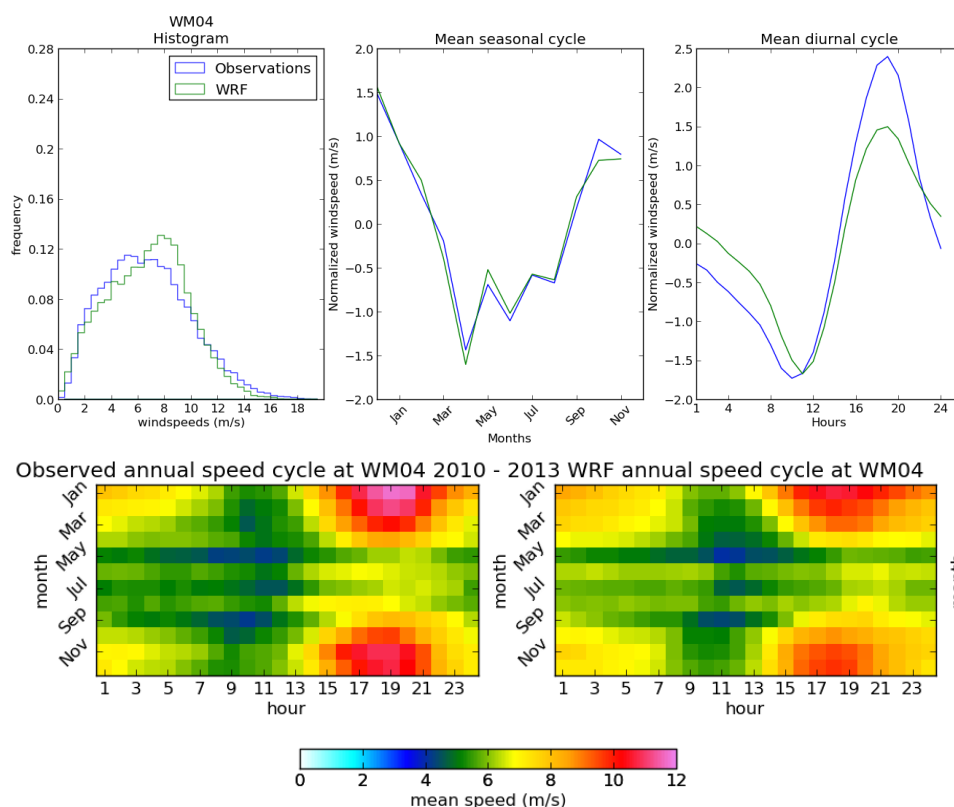

Figure 5.17 – Comparison of the wind speed $(\mathrm{m\,s^{-1}})$ at 62 m AGL at WM07: Wind speed distribution (top left), mean seasonal cycle (top center) and mean diurnal cycle (top right) in the mast measurements (blue) and in the WRF model simulations (green). Mean wind speed $(\mathrm{m\,s^{-1}})$ at 62 m AGL as a function of the time of the day (x-axis) and the month of the year (y-axis) for the mast observations (bottom left) and the WRF simulations (bottom right).

5.2.8 Humansdorp (WM08)

At WM08 (Fig. 5.18) the highest wind speeds are evident in the late morning and afternoon almost all year round. The model generally over-simulates austral autumn and winter wind speeds but under-simulates late austral spring and summer speeds. The shape of the diurnal cycle is captured but late night and early morning winds are over-simulated whereas daytime wind speeds are generally under-simulated. Therefore, the amplitude of the diurnal cycle of wind speed is underestimated in the WRF simulations compared to the observations. The low mean bias likely results from a cancellation of these errors.

There are errors in this data (December 2012) and there is also much missing data because of mast failure.
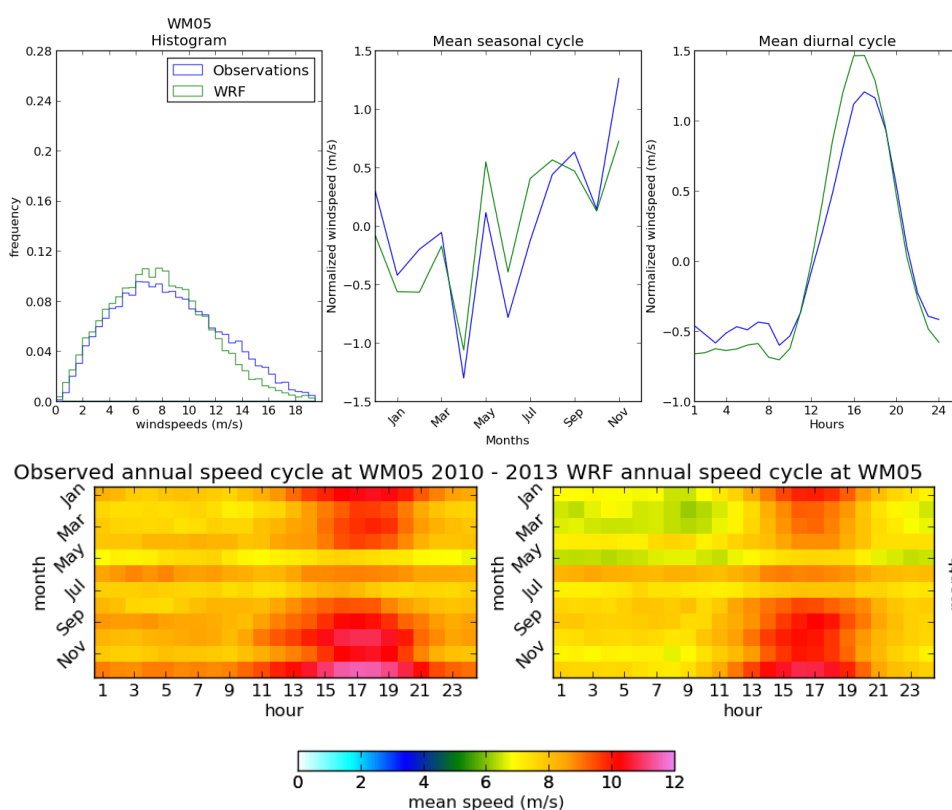

Figure 5.18 – Comparison of the wind speed ($\mathrm{m\,s^{-1}}$) at 62 m AGL at WM08: Wind speed distribution (top left), mean seasonal cycle (top center) and mean diurnal cycle (top right) in the mast measurements (blue) and in the WRF model simulations (green). Mean wind speed ($\mathrm{m\,s^{-1}}$) at 62 m AGL as a function of the time of the day (x-axis) and the month of the year (y-axis) for the mast observations (bottom left) and the WRF simulations (bottom right).

5.2.9   Noupoort (WM09)

Only one continuous year of data was available from this mast (2011) so it is therefore difficult to characterize the annual cycle of wind speed here. For the period a full year of measurements were available, highest wind speeds were measured throughout the day in austral winter and in the afternoon in spring. The model produced a higher frequency of wind speeds between 6–14 m s^{-1} and had a high positive mean bias. The model captures the seasonal cycle well but it must be noted this is only one year of observations. The diurnal cycle is generally well reproduced except in the late evening where simulated wind speeds are too high in almost all months. There are errors in this data (July, December 2011) and there is also much missing data because of mast failure.
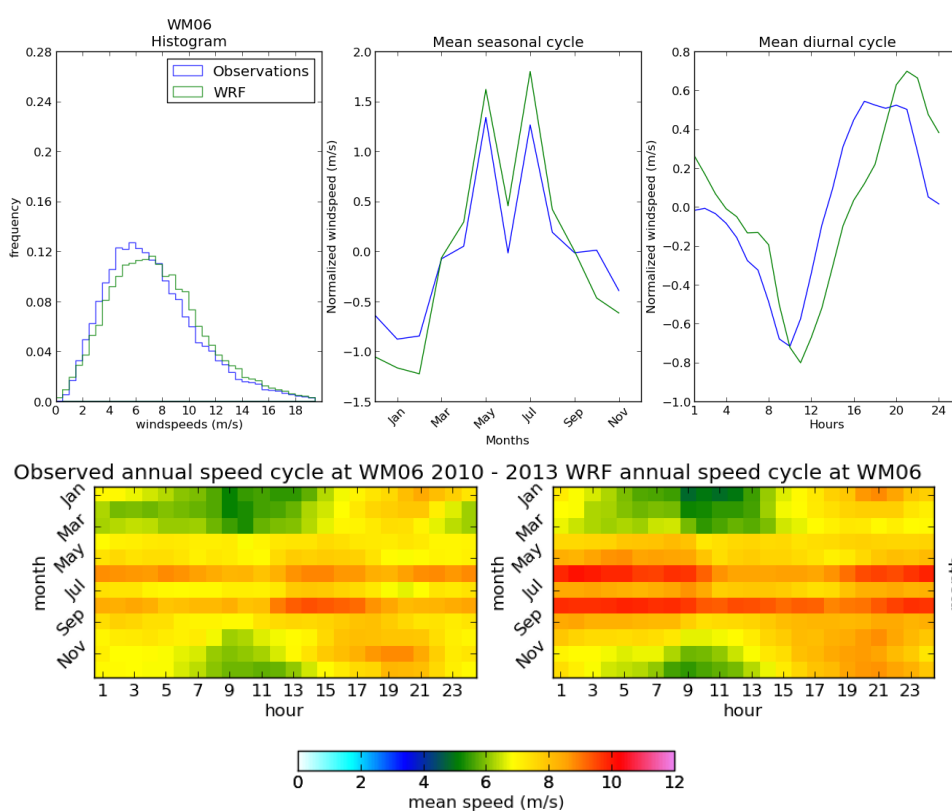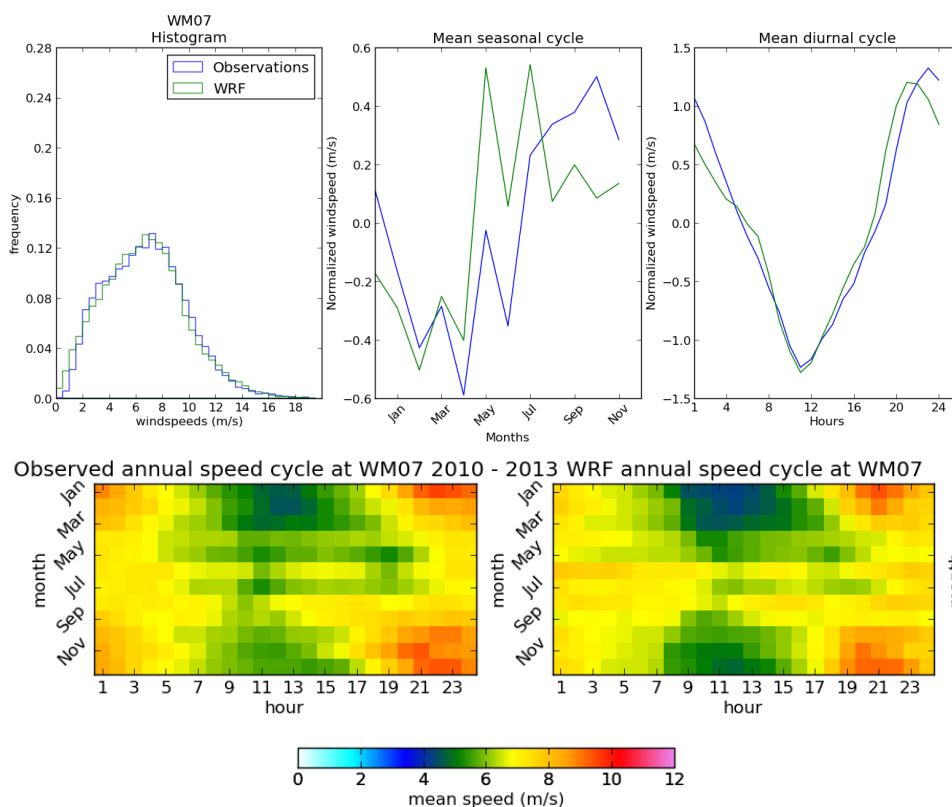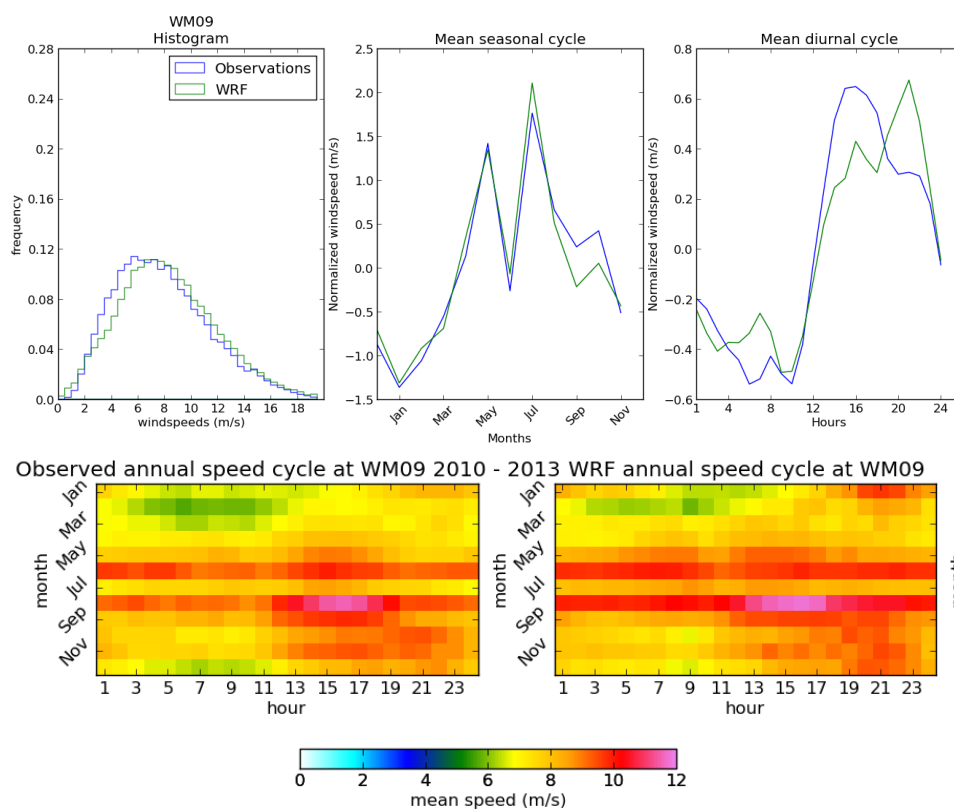

Figure 5.19 – Comparison of the wind speed (m s^{-1}) at 62 m AGL at WM09: Wind speed distribution (top left), mean seasonal cycle (top center) and mean diurnal cycle (top right) in the mast measurements (blue) and in the WRF model simulations (green). Mean wind speed (m s^{-1}) at 62 m AGL as a function of the time of the day (x-axis) and the month of the year (y-axis) for the mast observations (bottom left) and the WRF simulations (bottom right).

5.2.10   Butterworth (WM10)

Only one continuous year of data was available from this mast (2011) so it is therefore difficult to characterize the annual cycle of wind speed here. For the period a full year of measurements were available, highest wind speeds were measured in the afternoon with a maximum in the austral spring and summer. For the period a full year of measurements were available, highest wind speeds were generally measured in the afternoon with a maximum in June. The model

captures the shape of the the diurnal scale but over-simulates early morning wind speeds (largely a function of over-simulating June early morning wind speeds) and under-simulates the afternoon peak. The model also captures the shape of seasonal cycle well (in this year) although it over-simulates austral autumn and winter wind speeds and under-simulates austral spring and summer wind speeds.

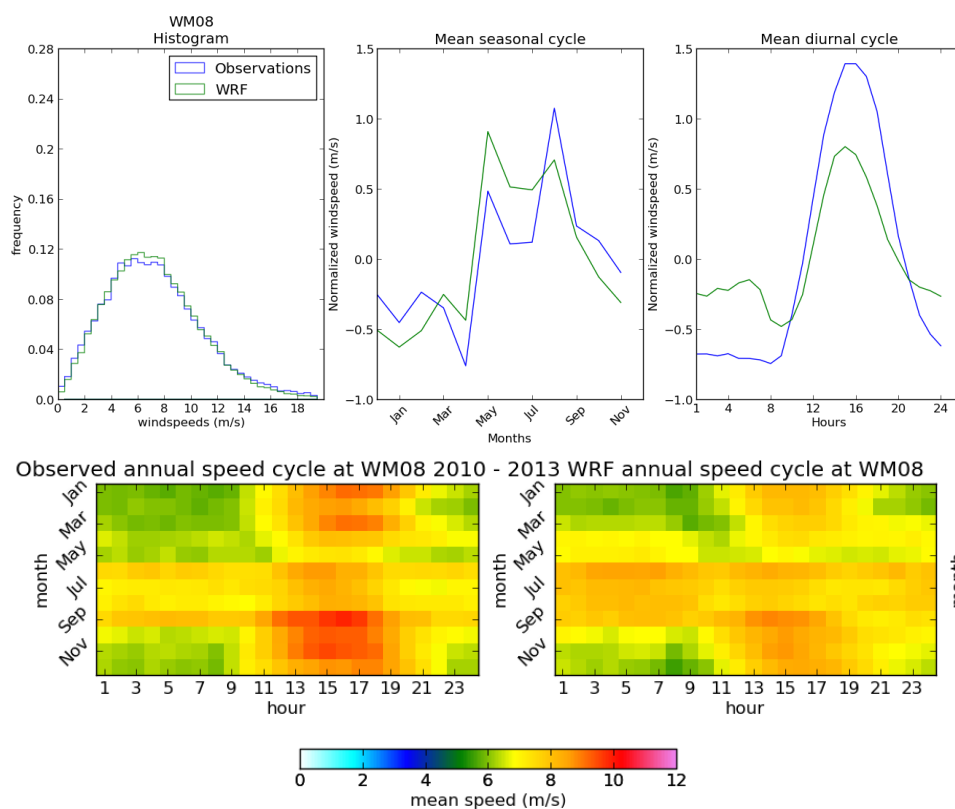There are missing data for March–May 2012 and June–August 2013.
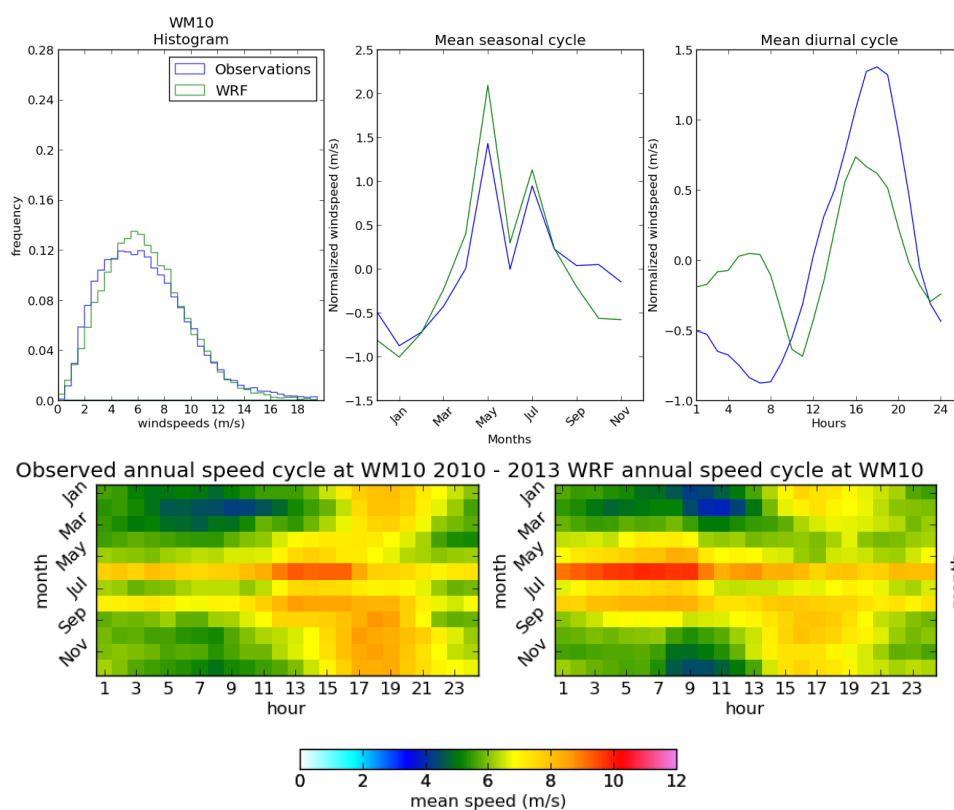
Figure 5.20 – Comparison of the wind speed ($m\,s^{-1}$) at 62 m AGL at WM10: Wind speed distribution (top left), mean seasonal cycle (top center) and mean diurnal cycle (top right) in the mast measurements (blue) and in the WRF model simulations (green). Mean wind speed ($m\,s^{-1}$) at 62 m AGL as a function of the time of the day (x-axis) and the month of the year (y-axis) for the mast observations (bottom left) and the WRF simulations (bottom right).

5.3   Other measured parameters

In addition to wind speed and wind direction, the WASA masts have instruments measuring temperature (at 60 m), temperature gradient (between 20 and 60 m), and relative humidity (at 60 m). Therefore, we present validation of two other parameters from the WRF simulations and the values at the 10 WASA masts.

In Fig. 5.21 the temperature gradient between 20–60 m is compared to that obtained from the WRF simulations. This comparison gives some insight into the representation of atmospheric stability by WRF. Overall the "tilt" of the temperature graphs shows that the range of temperature gradient simulated by WRF is smaller than that observed.
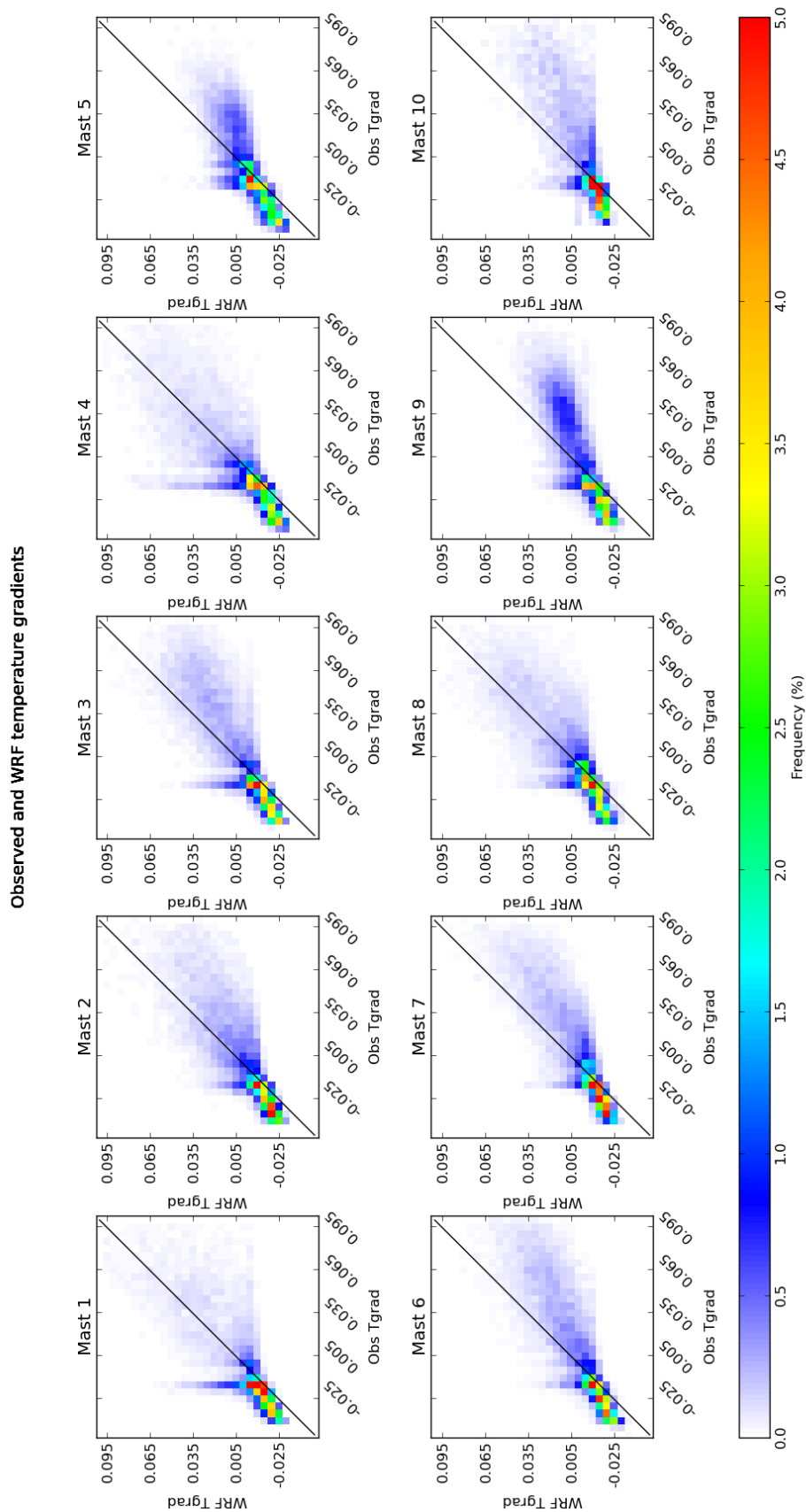
Figure 5.21 – Comparison of observed (x-axis) versus WRF-simulated (y-axis) 20–60 m temperature gradient (°C) for all 10 WASA sites.

Figure 5.22 compares the α-parameter (computed using Eq. 2.13) from the 20 and 60 m wind speeds at the mast and in the WRF simulations. The correspondence is quite good for most sites, except for WM04 and WM10. We speculate that the problems at these two sites are due to the misrepresentation of atmospheric stability at these sites.

Observed and WRF windshear
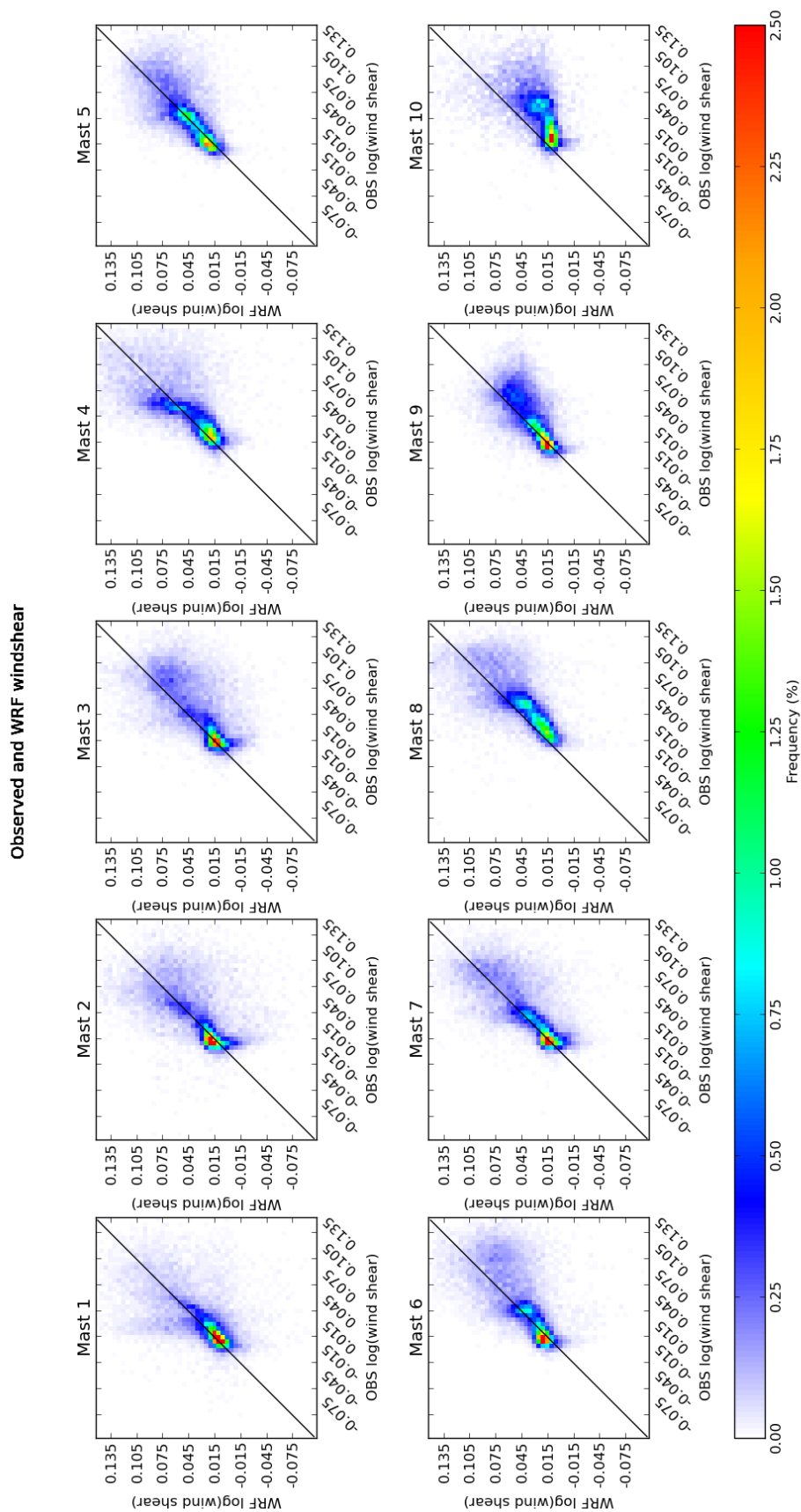
Figure 5.22 – Comparison of observed (x-axis) versus WRF-simulated (y-axis) 20–60 m wind shear exponent (α) for all 10 WASA sites.

Chapter 6

The numerical wind atlases

6.1 KAMM-WAsP NWA

Results of the combined domains for the KAMM-WAsP method (Fig. 3.3) are show in the following figures. In Figures 6.1 and 6.2 the 30-year simulated mean wind speed and power density at 100 m above surface level is shown. In Figures 6.3 and 6.4 the generalized 30-year wind climate is shown. The figures show 30-year generalized mean wind speed and power density at 100 m above flat terrain with a roughness length of 3 cm.
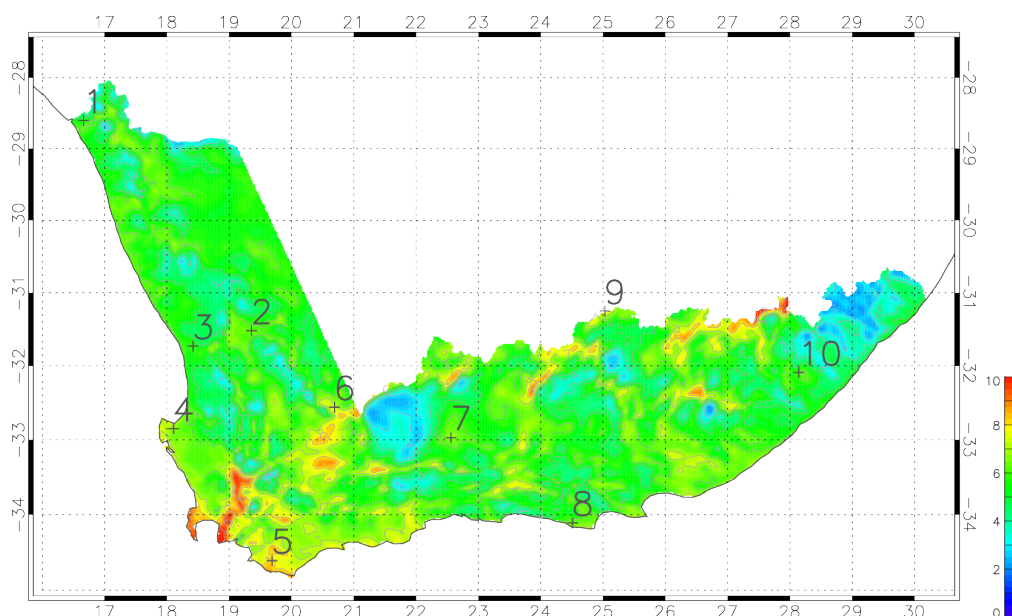
Figure 6.1 – Annual mean simulated wind speed at 100 m AGL. The colour scale to the right hand side is in $\mathrm{m\,s^{-1}}$. Axes are given in longitude and latitude coordinates.
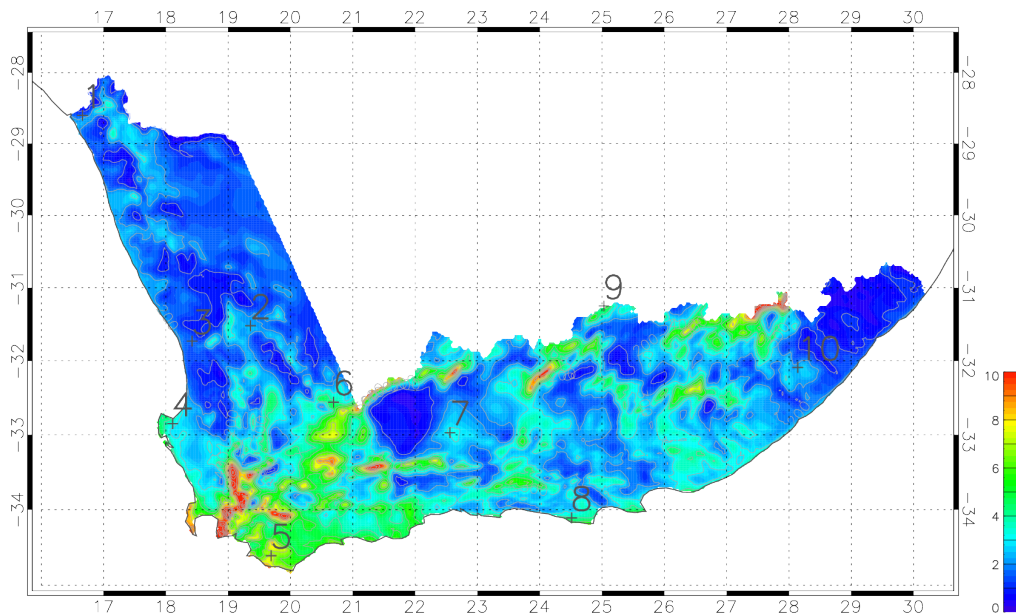
Figure 6.2 – Annual mean simulated wind power density at 100 m AGL. The colour scale to the right hand side is in $\mathrm{W\,m^{-2}}$. Axes are given in longitude and latitude coordinates.
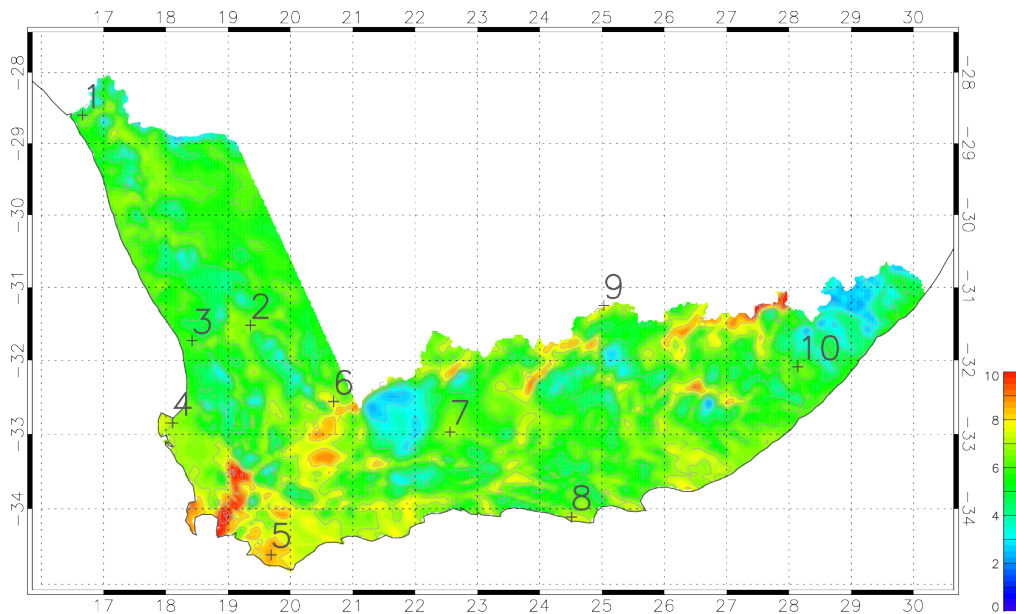
Figure 6.3 – Annual mean generalized wind speed at 100 m AGL for a flat homogeneous surface with roughness length 0.03 m. The colour scale to the right hand side is in $\mathrm{m\,s^{-1}}$. Axes are given in longitude and latitude coordinates.

63
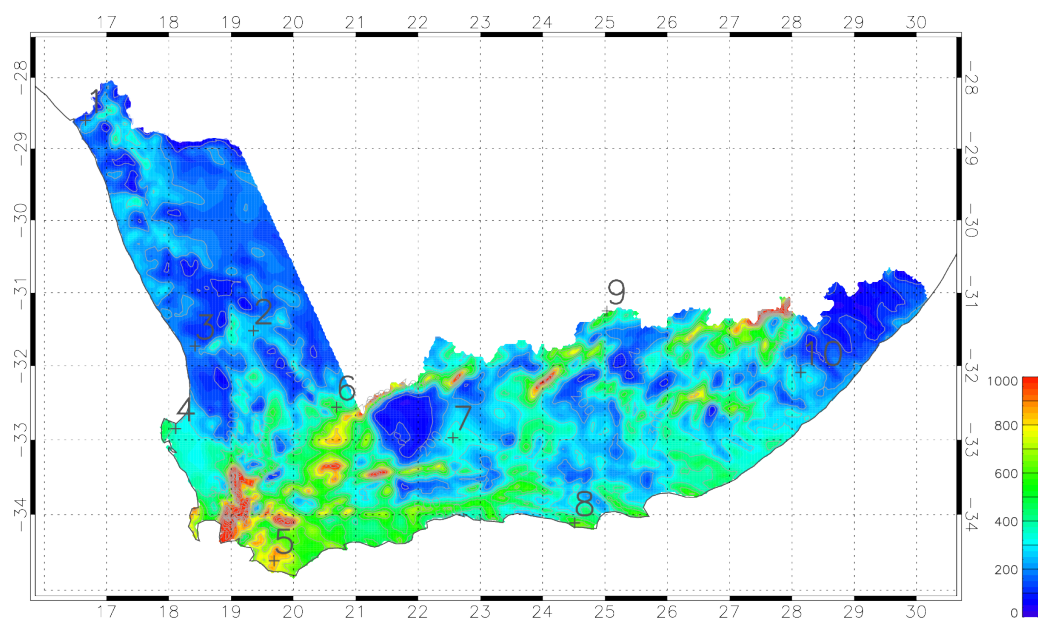
Figure 6.4 – Annual mean generalized wind power density at 100 m AGL for a flat homogeneous surface with roughness length 0.03 m. The colour scale to the right hand side is in $W \, m^{-2}$. Axes are given in longitude and latitude coordinates.

6.2 WRF-based NWA

Maps of the WRF-based numerical wind atlas are now presented. The averages correspond to the period of simulation 1 October 2005 – 30 September 2013.
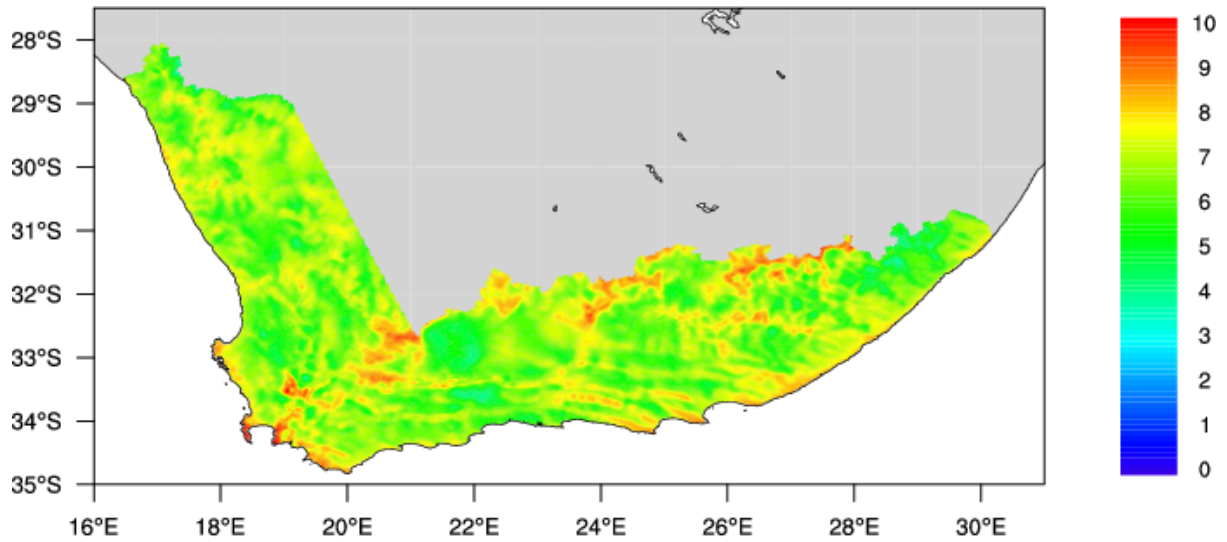
Figure 6.5 – Annual mean simulated wind speed at 100 m AGL from the WRF-based NWA. The color scale to the right hand side is in $\mathrm{m\,s^{-1}}$. Axes are given in longitude and latitude coordinates.
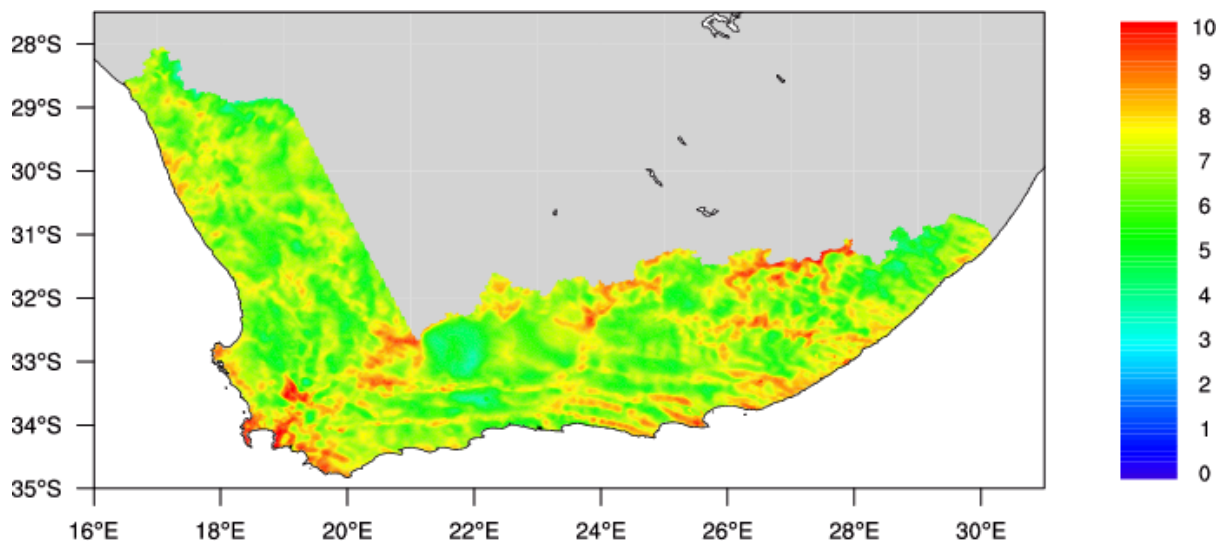
Figure 6.6 – Annual mean generalized wind speed at 100 m AGL from the WRF-based NWA. The color scale to the right hand side is in $\mathrm{m\,s^{-1}}$. Axes are given in longitude and latitude coordinates.
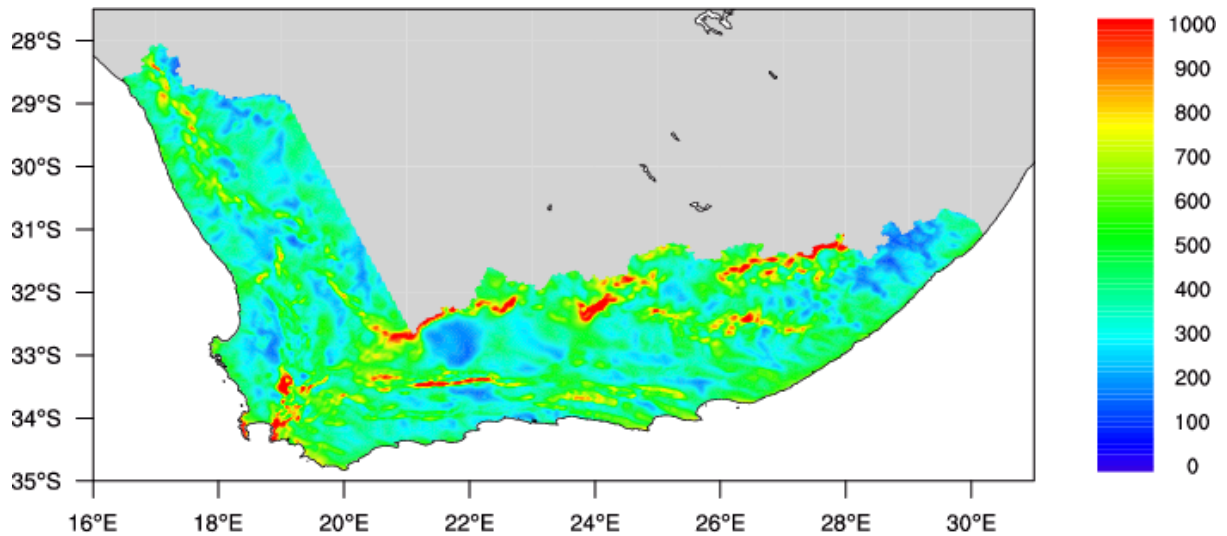
Figure 6.7 – Annual mean simulated wind power density at 100 m AGL from the WRF-based NWA. The color scale to the right hand side is in $W\,m^{-2}$. Axes are given in longitude and latitude coordinates.
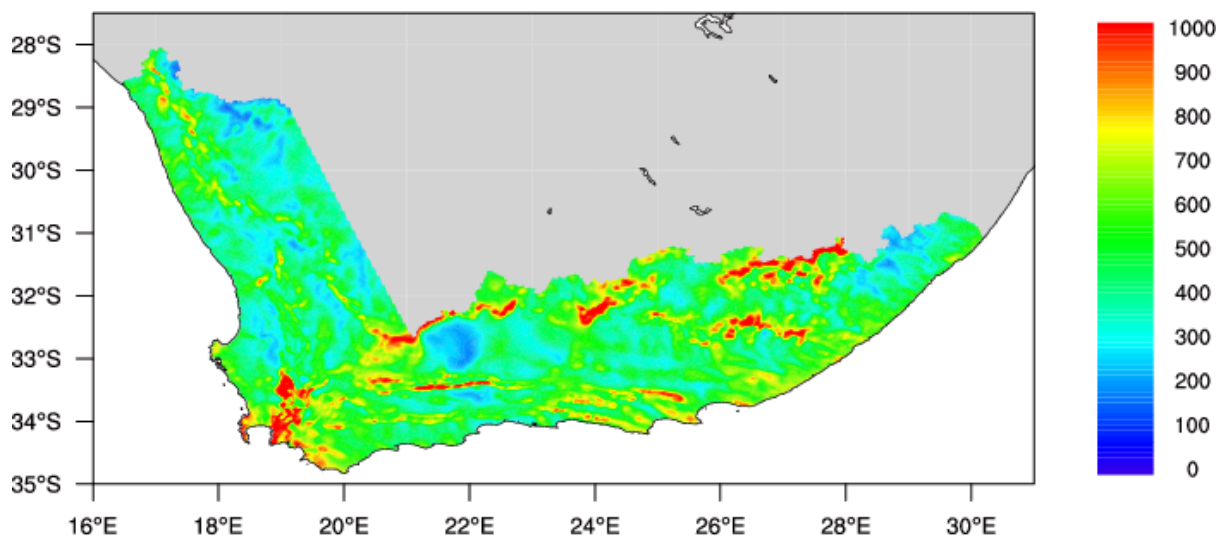
Figure 6.8 – Annual mean generalized wind power density at 100 m AGL from the WRF-based NWA. The color scale to the right hand side is in $W\,m^{-2}$. Axes are given in longitude and latitude coordinates.

Chapter 7

Summary and conclusions

The first part of this report has described two methodologies for the generation of wind resource estimates over a large area in the absence of sufficient quality measurement data. Both methods the KAMM-WAsP- and the WRF- methods are based on NWP technology. The first method is on simulations from the KAMM model, driven by representative wind classes classified from the reanalysis data. The output from KAMM is generalized by the removal of surface effects, as they are seen in the model, yielding a generalized wind climate over the area of interest. These simulations have been conducted at 5 km resolution for three domains covering the WASA domain.

The second methodology, the WRF mesoscale analysis method, utilizes the WRF mesoscale model to directly simulate atmospheric conditions over the region surrounding the WASA domain. As for the KAMM-WAsP method, the results are generalized for each location of interest, by the removal of the effects of the surface, as seen by the mesoscale model. This statistical analysis results in Weibull distributions and wind roses for the generalized climate, at a standard height and roughness, at these locations. These simulations have been run for the period of 8 years, October 2005 – September 2013, at high resolution (3 km inner grid).

The second part compares the results from the numerical wind atlases (NWA) produced by the KAMM-WAsP and WRF methods and verifies the two wind atlas from the two methods against observed wind atlas (OWA) generated from data from the 10 WASA masts. The KAMM-WAsP method was found to underestimate the generalized mean wind speeds at the sites (mean bias of -8.2% and an mean absolute bias of 9.3%). In the WRF-based method there is, on average, a difference of 4.6% (either positive or negative) between the WRF-based NWA results and the corresponding observed values. The combined average across all the sites is an over-estimate of 2.3%.

Each method results in slightly different estimates of the wind climate, allowing a preliminary assessment of the uncertainty associated with these estimates at each site investigated. The lack of thermally driven forcing (e.g. sea-land and valley breezes) in the KAMM modeling is probably responsible for most of the discrepancies.

7.1   Error and uncertainty

Many factors contribute to the uncertainty of the results. A few known sources errors in the WRF-based wind atlas are listed below:

1. Uncertainty in the forcing reanalysis:
   Due to the sparse observing system, the ERA-Interim reanalysis is expected to contain larger errors in Southern Africa than in other parts of the world. These errors directly impact the quality of the WRF analyses. However, the fact that simulations using a different reanalysis provide similar results (see Fig. 4.2a), suggest that the errors relating to the reanalysis are small. In other regions, differences in mean wind speed due to various reanalysis are also quite small ($< 3\%$ in the 100 m mean wind speed) in the North and Baltic Seas (Hahmann et al., 2012).

2. Uncertainty in the WRF simulations:
   The veracity of the WRF simulations themselves, and how these vary with the various setting in the simulations, will introduce errors in the final wind atlas. For example, for the North and Baltic Seas, changing the boundary layer scheme can introduce differences in mean wind speed of the order of 0.4 m s^{-1} or $\sim 7\%$ (Hahmann et al., 2012). The sensitivity experiments presented in section 4 (see Fig. 4.2b) show, however, that the wind climate simulated by WRF is quite insensitive to most of these choices including the choice of PBL scheme.

3. Representativeness of the simulated period:
   An additional error is introduced in the estimates derived from the WRF simulations because only eight years (1 October 2005 to 30 September 2013) are used. This error is expected to be small, however, to quantify it, an analysis of the representativeness of these 8 years in the long-term wind climatology will have to be carried out.

4. Errors in the generalization method:
   The generalization method used was originally developed for use within the KAMM model infrastructure (see section 3.1). We later adapted it for use with the WRF model output, and, because the models and the simulating methods are different in the two models, additional errors can be introduced.

Bibliography

Adrian, G. and F. Fiedler, 1991: Simulation of unstationary wind and temperature fields over complex terrain and comparison with observations. *Beitr. Phys. Atmosph.*, **64**, 27–48.

Badger, J., H. Frank, A. N. Hahmann, and G. Giebel, 2014: Wind-Climate Estimation Based on Mesoscale and Microscale Modeling: Statistical-Dynamical Downscaling for Wind Energy Applications. *J. Appl. Meteorol. Climatol.*, **53**, 1901–1919.
URL http://journals.ametsoc.org/doi/abs/10.1175/JAMC-D-13-0147.1

Deacon, E. L., 1973: Geostrophic drag coefficients. *Boundary-Layer Meteorol.*, **5**, 321–340.

Dee, D. P., S. M. Uppala, A. J. Simmons, P. Berrisford, P. Poli, S. Kobayashi, U. Andrae, M. A. Balmaseda, et al., 2011: The ERA-Interim reanalysis: configuration and performance of the data assimilation system. *Q. J. R. Meteorolog. Soc.*, **137**, 553–597.

Draxl, C., A. N. Hahmann, A. Peña, and G. Giebel, 2014: Evaluating winds and vertical wind shear from WRF model forecasts using seven PBL schemes. *Wind Energy*, **17**, 39–55.

Floors, R., 2013: Measuring and modelling of the wind on the scale of tall wind turbines. PhD-0034(EN). Phd, Technical University of Denmark.

Frank, H. and L. Landberg, 1997: Modelling the wind climate of Ireland. *Bound.-Layer Meteor.*, **85**, 359–378.

Frey-Buness, F., D. Heimann, and R. Sausen, 1995: A statistical-dynamical downscaling procedure for global climate simulations. *Theor. Appl. Climatol.*, **50**, 117–131.

Friedl, M. A., D. Sulla-Menashe, B. Tan, A. Schneider, N. Ramankutty, A. Sibley, and X. Huang, 2010: MODIS Collection 5 global land cover: Algorithm refinements and characterization of new datasets. *Remote Sens. Environ.*, **114**, 168–182.
URL http://www.sciencedirect.com/science/article/pii/S0034425709002673

Gemmill, W., B. Katz, and X. Li, 2007: Daily real-time global sea surface temperature - high resolution analysis at NOAA/NCEP. Office note nr. 260, 39 pp, NOAA/NWS/NCEP/MMAB.

Gill, A. E., 1968: Similarity theory and geostrophic adjustment. *Q. J. R. Meteorol. Soc.*, **94**, 586–588.

Hahmann, A. N., J. Lange, and A. Peña, 2012: The NORSEWInD numerical wind atlas for the South Baltic. Tech. Rep. November, DTU Wind Energy.

Hahmann, A. N., D. Rostkier-Edelstein, T. T. Warner, F. Vandenberghe, Y. Liu, R. Babarsky, and S. P. Swerdlin, 2010: A Reanalysis System for the Generation of Mesoscale Climatographies. *J. Appl. Meteor. Clim.*, **49**, 954–972.

Horvath, K., D. Koracin, R. Vellore, J. Jiang, and R. Belu, 2012: Sub-kilometer dynamical downscaling of near-surface winds in complex terrain using WRF and MM5 mesoscale models. *J. Geophys. Res.*, **117**, D11 111.

Kelly, M. and I. Troen, 2014: Probabilistic stability and "tall" wind profiles: theory and method for use in wind resource assessment. *Wind Energy*, **in press**.

Kristensen, L. and G. Jensen, 1999: Geostrophic winds in Denmark : a preliminary study. Risø-R-1145(EN). Tech. Rep. November, Risø National Laboratory, Roskilde, Denmark.

Larsén, X. G., J. Badger, A. N. Hahmann, and N. G. Mortensen, 2013: The selective dynamical downscaling method for extreme-wind atlases. *Wind Energy*, **16**, 1167–1182.

Larsén, X. G., S. Larsen, and A. N. Hahmann, 2012: Origin of the waves in A case-study of mesoscale spectra of wind and temperature, observed and simulated': Lee waves from the Norwegian mountains. *Q. J. R. Meteorolog. Soc.*, **138**, 274–279.

Mellor, G. L. and T. Yamada, 1982: Development of a turbulence closure model for geophysical fluid problems. *Rev. Geophys. and Space Phys.*, **20**, 851–875.

Mortensen, N., J. C. Hansen, M. C. Kelly, E. Prinsloo, E. Mabille, and S. Szewczuk, 2014a: Wind Atlas for South Africa (WASA) - Station and Site Description Report. Tech. rep., Department of Wind Energy, Technical University of Denmark (DTU) and Council for Scientific and Industrial Research (CSIR).

Mortensen, N. G., J. C. Hansen, M. C. Kelly, S. Szewczuk, E. Mabille, and E. Prinsloo, 2014b: Wind Atlas for South Africa (WASA) - Observational wind atlas for 10 met. stations in Northern, Western and Eastern Cape provinces. Tech. rep., Department of Wind Energy, Technical University of Denmark (DTU) and Council for Scientific and Industrial Research (CSIR).

Mortensen, N. G., O. Rathmann, L. Landberg, G. Jensen, and E. Petersen, 1999: Wind atlas analysis of 26 Danish stations (1987–96). Tech. Rep. Risø-R-1092, Risø National Laboratory (unpublished).

Peña, A. and A. N. Hahmann, 2012: Atmospheric stability and turbulence fluxes at Horns Rev — An intercomparison of sonic, bulk and WRF model data. *Wind Energy*, **15**, 717–731.

Skamarock, W. C., J. B. Klemp, J. Dudhia, D. O. Gill, D. M. Barker, M. G. Duda, X.-Y. Huang, W. Wang, et al., 2008: A Description of the Advanced Research WRF Version 3. Tech. Rep. NCAR/TN–475+STR, National Center for Atmospheric Research.

Storm, B., J. Dudhia, S. Basu, A. Swift, and I. Giammanco, 2009: Evaluation of the weather research and forecasting model on forecasting low-level jets: implications for wind energy. *Wind Energy*, **12**, 81–90.

Troen, I. and E. L. Petersen, 1989: *European Wind Atlas*. Published for the Commission of the European Communities, Directorate-General for Science, Research, and Development, Brussels, Belgium by Risø National Laboratory.

Tuller, S. E. and A. C. Brett, 1984: The characteristics of wind velocity that favor the fitting of a Weibull distribution in wind-speed analysis. *J. Appl. Meteor. Clim.*, **23**, 124–134.

Vincent, C. L., A. N. Hahmann, and M. C. Kelly, 2012: Idealized mesoscale model simulations of open cellular convection over the sea. *Bound.-Layer Meteor.*, **142**, 103–121.

Appendix A

WRF namelist

```
&time_control
interval_seconds                    = 21600,
input_from_file                     = .T., .T., .T.,
history_interval                    = 180,180, 60,
frames_per_outfile                  =   1,  1,   3,
restart                             = .false.,
restart_interval                    = 100000,
io_form_history                     = 2
io_form_restart                     = 2
io_form_input                       = 2
io_form_boundary                    = 2
auxhist3_outname                    = "winds_d<domain>_<date>",
auxhist3_interval                   = 0, 0, 10,
frames_per_auxhist3                 = 1, 1,   6,
io_form_auxhist3                    = 2,
auxinput4_inname                    = "wrflowinp_d<domain>",
auxinput4_interval                  = 360,360,360,
io_form_auxinput4                   = 2,
iofields_filename                   = "WAfields.txt","WAfields.txt","WAfields.txt",
/

&domains
time_step                           = 163,
time_step_fract_num                 = 14,
time_step_fract_den                 = 22,
max_dom                             = 3,
s_we                                =  1,    1,    1,
e_we                                = 90, 184, 436,
s_sn                                =  1,    1,    1,
e_sn                                = 70, 133, 310,
s_vert                              =  1,    1,    1,
e_vert                              = 41,   41,   41,
grid_id                             =  1,    2,    3,
```

```
parent_id                        =  0,    1,    2,
i_parent_start                   =  1,   18,   25,
j_parent_start                   =  1,   14,   13,
num_metgrid_levels               = 38,
p_top_requested                  = 5000,
eta_levels   = 1.0000, 0.9965, 0.9930, 0.9895, 0.9860,
               0.9825, 0.9714, 0.9539, 0.9308, 0.9034,
               0.8724, 0.8388, 0.8034, 0.7669, 0.7298,
               0.6926, 0.6558, 0.6196, 0.5842, 0.5499,
               0.5168, 0.4848, 0.4540, 0.4244, 0.3958,
               0.3683, 0.3417, 0.3158, 0.2906, 0.2659,
               0.2415, 0.2174, 0.1934, 0.1694, 0.1453,
               0.1212, 0.0969, 0.0698, 0.0454, 0.0215,
               0.000
dx                               = 27000, 9000, 3000,
dy                               = 27000, 9000, 3000,
parent_grid_ratio                = 1,    3,     3,
parent_time_step_ratio           = 1,    3,     3,
feedback                         = 0,
smooth_option                    = 0,
/


&physics
mp_physics                       =  4,   4,   4,
ra_lw_physics                    =  1,   1,   1,
ra_sw_physics                    =  1,   1,   1,
radt                             = 10,  10,  10,
sf_sfclay_physics                =  2,   2,   2,
sf_surface_physics               =  2,   2,   2,
bl_pbl_physics                   =  2,   2,   2,
bldt                             =  0,   0,   0,
cu_physics                       =  1,   1,   0,
cudt                             =  5,   5,   5,
fractional_seaice                = 1,
seaice_threshold                 = 0.,
isfflx                           = 1,
ifsnow                           = 0,
icloud                           = 1,
surface_input_source             = 1,
num_land_cat                     = 20,
num_soil_layers                  = 4,
sst_update                       = 1,
maxiens                          = 1,
maxens                           = 3,
maxens2                          = 3,
maxens3                          = 16,
```

```
ensdim                          = 144,
/

&fdda
grid_fdda                       = 1,      0,     0,
gfdda_inname                    = "wrffdda_d<domain>",
gfdda_end_h                     = 264,    0,     0,
gfdda_interval_m                = 360,    0,     0,
fgdt                            = 0,      0,     0,
if_no_pbl_nudging_uv            = 0,      0,     0,
if_no_pbl_nudging_t             = 1,      0,     0,
if_no_pbl_nudging_q             = 1,      0,     0,
if_zfac_uv                      = 1,      0,     0,
 k_zfac_uv                      = 15,     0,     0,
if_zfac_t                       = 1,      0,     0,
 k_zfac_t                       = 15,     0,     0,
if_zfac_q                       = 1,      0,     0,
 k_zfac_q                       = 15,     0,     0,
guv                             = 0.0003, 0.000075, 0.000075,
gt                              = 0.0003, 0.000075, 0.000075,
gq                              = 0.0003, 0.000075, 0.000075,
if_ramping                      = 0,
dtramp_min                      = 60.0,
io_form_gfdda                   = 2,
/

&dynamics
w_damping                       = 1,
diff_opt                        = 1,
km_opt                          = 4,
diff_6th_opt                    = 2,     2,     2,    2,
diff_6th_factor                 = 0.06, 0.08, 0.1, 0.1,
base_temp                       = 290.
damp_opt                        = 0,
zdamp                           = 5000., 5000., 5000.,
dampcoef                        = 0.15,  0.15,  0.15,
khdif                           = 0,      0,     0,
kvdif                           = 0,      0,     0,
non_hydrostatic                 = .true.,.true.,.true.,
moist_adv_opt                   = 1,      1,     1,
scalar_adv_opt                  = 1,      1,     1,
/

&bdy_control
spec_bdy_width                  = 5,
spec_zone                       = 1,
```

```
relax_zone                        = 4,
specified                         = .true., .false.,.false.,
nested                            = .false., .true., .true.,
/
```

DTU Wind Energy is a department of the Technical University of Denmark with a unique integration of research, education, innovation and public/private sector consulting in the field of wind energy. Our activities develop new opportunities and technology for the global and Danish exploitation of wind energy. Research focuses on key technical-scientific fields, which are central for the development, innovation and use of wind energy and provides the basis for advanced education at the education.

We have more than 240 staff members of which approximately 60 are PhD students. Research is conducted within nine research programmes organized into three main topics: Wind energy systems, Wind turbine technology and Basics for wind energy.